

2-D MODELING OF COMPRESSION IGNITION ENGINE COMBUSTION

by

Cebrail Yıldırım

B.S., Mechanical Engineering, Istanbul Technical University, 2012

Submitted to the Institute for Graduate Studies in
Science and Engineering in partial fulfillment of
the requirements for the degree of
Master of Science

Graduate Program in Mechanical Engineering
Boğaziçi University

2016

2-D MODELING OF COMPRESSION IGNITION ENGINE COMBUSTION

APPROVED BY:

Assoc. Prof. Hasan BEDİR
(Thesis Supervisor)

Assoc. Prof. Kunt ATALIK

Prof. Ramazan YILDIRIM

DATE OF APPROVAL: 29.12.2015

ACKNOWLEDGEMENTS

I would like to express my appreciation to my supervisor Assoc. Prof. Hasan Bedir for his guidances and advices from the beginning to the end of this study. I am also thankful to Assoc. Prof. Kunt ATALIK and Prof. Ramazan YILDIRIM for participating to my thesis presentation. Besides, I would also like to thank to Alpay, Msc. and Oğuz, Msc. for giving me support and sharing their experiences and knowledges which dramatically paced up the study. Moreover, I am thankful to my girlfriend, Gülsevim, for always pushing me forward, motivating me and finally making it possible for me to complete my studies successfully. I should also say my thanks to Göker, Oğuzhan and Yasin for their friendships. Finally, I would really like to express my gratitudes to my family for always being with me and always giving support.

ABSTRACT

2-D MODELING OF COMPRESSION IGNITION ENGINE COMBUSTION

Internal combustion engines are the cornerstones of our society. They are widely used in a vast range of area from transportation to power generation. Since they are mostly petroleum-powered and emission regulations are getting tighter due to the environmental concerns, ICE research activity is vibrant today. In the present study, a multidimensional CFD approach has been used to simulate a CI diesel engine combustion to investigate the effect of injection timing and swirl ratio on combustion and emissions. AVL Fire software has been used for combustion, spray and emission modeling. Within this context, ECFM-3Z, $k - \epsilon$, Wave break-up, Dukowicz, extended Zeldovich and Hiroyasu approaches have been used for, in order, combustion, turbulence, spray atomization, spray evaporation, NO_x and soot emission modeling. When compared with the experimental data, the simulation results show a good agreement. As for the swirl ratios, minimum NO and soot emission are achieved at SR 3.0 while the optimum bsfc and maximum indicated efficiency are found at SR 1.0. Findings of different injection timing are that advanced injection results in higher NO and higher soot emissions as the retarded injection provides lower NO and higher soot emissions with reference to the baseline simulation.. As a result, SR 1.0 and reference injection timing have been found to be the optimum configuration in terms of bsfc and emissions for the engine studied.

ÖZET

2-B SIKIŞTIRMALI ATEŞLEMELİ MOTOR YANMA MODELLEMESİ

Ulaşımından güç üretimine kadar yaygın olarak kullanılan içten yanmalı motorlar, bugün toplumumuzda önemli bir yere sahiptir. Yakıt olarak çoğunlukla petrol ürünlerinin kullanılması, çevresel kaygılardan dolayı sürekli olarak daha da sıkı hale getirilen emisyon standartlarından ötürü içten yanmalı motorlar üzerine araştırma ve geliştirme çalışmaları günümüzde oldukça yaygındır. Bu çalışmada, enjeksiyon zamanı ve girdap oranı gibi parametrelerin yanma ve emisyon üzerine etkisinin incelenmesi için çok boyutlu hesaplamalı akışkan dinamiği (CFD) yaklaşımı, sıkıştırımlı ateşlemeli dizel bir motor için uygulanmıştır. AVL Fire yazılımının kullanıldığı çalışmada, ECFM-3Z, $k - \epsilon$, Wave break-up, Dukawicz, extended Zeldovich ve Hiroyashu yaklaşımları, sırasıyla, yanma, türbilans, sprey atomizasyonu, sprey buharlaşması, NO_x ve kurum emisyonları modellemelerinde kullanılmıştır. Similasyon sonuçları deneysel verilerle uygunluk göstermiştir. Girdap oranları değerlendirildiğinde, daha düşük NO ve kurum emisyonları girdap oranı(SR) 3.0 için, minimum yakıt sarfiyatı ve verim girdap oranı 1.0 için gözlenmiştir. Enjeksiyon zamanlaması çalışmalarında ise erken enjeksiyonun daha yüksek NO ve daha düşük kurum emisyonlarına sebep olduğu gözlenmiştir. Geç enjeksiyon similasyonlarında ise daha düşük NO ve daha yüksek kurum emisyonları gözlenmiştir. Sonuç olarak, üzerinde çalışılan motor için girdap oranı 1.0 ve referans enjeksiyon uygulanması optimum yakıt sarfiyatı ve emisyon salınımı sağlamıştır.

TABLE OF CONTENTS

ACKNOWLEDGEMENTS	iii
ABSTRACT	iv
ÖZET	v
LIST OF FIGURES	viii
LIST OF TABLES	xi
LIST OF SYMBOLS	xii
LIST OF ACRONYMS/ABBREVIATIONS	xvii
1. INTRODUCTION	1
2. INTERNAL COMBUSTION ENGINES	6
2.1. Engine Operating Cycles	6
2.2. Engine Design and Operating Parameters	6
2.2.1. Compression Ratio	8
2.2.2. Brake Torque and Power	8
2.2.3. Mean Effective Pressure	9
2.2.3.1. Indicated Mean Effective Pressure	9
2.2.3.2. Friction Mean Effective Pressure	9
2.2.3.3. Auxiliary Drives Mean Effective Pressure	10
2.2.3.4. Break Mean Effective Pressure	10
2.2.4. Air-Fuel and Fuel-Air Ratios	10
2.2.5. Excess Air Ratio	11
2.2.6. Equivalence Ratio	11
2.2.7. Swirl Ratio	11
3. STUDIES IN THE LITERATURE	12
4. MATHEMATICAL APPROACH TO ICE MODELING	17
4.1. Combustion Models	18
4.1.1. Eddy Break-Up Model	20
4.1.2. Characteristic Timescale Model	20
4.1.3. Coherent Flame Model	22
4.1.3.1. Extended Coherent Flame Model(ECFM)	24

4.1.3.2.	Extended Coherent Flame Model 3-Zones(ECFM-3Z)	27
4.2.	Emission Models	29
4.2.1.	Extenden Zeldovich Mechanism for NO _x Modeling	29
4.2.2.	Soot Formation and The Hiroyasu/Nagle/Strickland-Constable Model	31
4.3.	Spray Models	32
4.3.1.	Mathematical Equations	33
4.3.2.	Evaporation Model	35
4.3.3.	Wave Break-up Model	37
4.3.4.	Turbulence Model	38
5.	SIMULATION AND RESULTS	39
5.1.	Geometrical Description	39
5.1.1.	Injector Geometry	40
5.1.2.	Final Geometry	40
5.2.	Domain Discretization	41
5.3.	Simulation Parameters	43
5.3.1.	Run Mode	43
5.3.2.	Base-Line Simulation	43
5.3.2.1.	Boundary Conditions	44
5.3.2.2.	Initial Conditions	44
5.3.2.3.	Simulation Models	44
5.3.3.	Validation of Base-line Simulation	45
5.3.3.1.	Quantity Plots for Base-line Simulation at 3600 rpm	49
5.3.3.2.	2D Countours at 3600 rpm	49
5.4.	Investigation on the Effects of Various Swirl Ratio and Injection Timing on Combustion and Emissions	51
5.4.1.	Simulation Results for Swirl Ratio	51
5.4.2.	Simulation Results for Injection Timing	59
6.	CONCLUSION AND FUTURE WORK	65
	REFERENCES	68

LIST OF FIGURES

Figure 1.1.	World motor vehicle production [1].	1
Figure 1.2.	Energy losses for gasoline vehicles [2].	3
Figure 2.1.	The four-stroke operating cycle [3].	7
Figure 2.2.	Geometry of cylinder and piston [3].	7
Figure 2.3.	Schematic of principle of operation of dynamometer.	8
Figure 3.1.	EGR system [4].	13
Figure 4.1.	Example of a discretization for in-cylinder.	17
Figure 4.2.	Conventional diesel engine combustion stages [5].	19
Figure 4.3.	Zones in ECFM 3Z.	27
Figure 4.4.	Regions for NO and soot emissions (Equivalence ratio) [6].	32
Figure 4.5.	Stages of high-pressure diesel spray breakup [7].	33
Figure 4.6.	Injection-rate shape map [5].	34
Figure 5.1.	Injector template.	40
Figure 5.2.	In cylinder computational domain.	41

Figure 5.3.	Mesh blocks in the computational domain.	42
Figure 5.4.	Engine power curve.	43
Figure 5.5.	Baseline heat release rate curve at 3600rpm.	46
Figure 5.6.	Baseline pressure curve at 3600rpm.	47
Figure 5.7.	Baseline temperature curve at 3600rpm.	47
Figure 5.8.	Baseline heatflux curve at 3600rpm.	48
Figure 5.9.	Baseline NO curve at 3600rpm.	48
Figure 5.10.	Baseline soot curve at 3600rpm.	49
Figure 5.11.	Baseline local pressures at 732 CA.	51
Figure 5.12.	Baseline local temperatures at 732 CA.	52
Figure 5.13.	Quantity contours at 720 CA.	52
Figure 5.14.	Quantity contours at 732 CA.	53
Figure 5.15.	Quantity contours at 738 CA.	54
Figure 5.16.	Quantity contours at 750 CA.	55
Figure 5.17.	Pressure curves for various swirl ratios.	55
Figure 5.18.	Temperature curves for various swirl ratios.	56

Figure 5.19. Rate of heat release curves for various swirl Ratios.	56
Figure 5.20. Burnt fuel mass fraction curves for various swirl ratios.	57
Figure 5.21. NO mass fraction curves for various swirl ratios.	57
Figure 5.22. Soot mass fraction curves for various swirl ratios.	58
Figure 5.23. Pressure curves for various injection timings.	61
Figure 5.24. Temperature curves for various injection timings.	61
Figure 5.25. Rate of heat release curves for various injection timing.	62
Figure 5.26. Accumulated heat release for various injection timing.	62
Figure 5.27. NO mass fraction curves for various injection timing.	63
Figure 5.28. Soot mass fraction curves for various injection timing.	63
Figure 6.1. SMD for various swirl ratios [8].	66

LIST OF TABLES

Table 4.1.	NOx model reaction rate constants.	30
Table 4.2.	Turbulence model constants	38
Table 5.1.	General engine configurations.	39
Table 5.2.	General injector parameters.	40
Table 5.3.	Mesh data.	42
Table 5.4.	Boundary conditions at 3600rpm.	44
Table 5.5.	Initial conditions at 3600rpm.	44
Table 5.6.	General engine output for 3600 rpm (Baseline).	46
Table 5.7.	Summary of the parametric study.	53
Table 5.8.	General engine output comparison for swirl ratio.	54
Table 5.9.	General engine output comparison for injection timing.	64
Table 6.1.	Average convective wall heat flux for SR cases.	66

LIST OF SYMBOLS

A_f	Soot formation constant
A_o	Soot oxidation constant
b	Dynamometer rod length
B	Bore diameter
B_y	Mass transfer number
c	Reaction progress variable
C_k	Turbulent flame stretch multiplier
c_{pd}	Heat capacity of droplet
C_D	Drag coefficient
C_{fu}	Combustion fuel constant
C_{Pr}	Combustion product constant
D_d	Droplet diameter
$D_{k,m}$	Diffusion coefficient of species k
E_a	Activation energy
E_{sf}	Activation energy for soot formation
E_{so}	Activation energy for soot oxidation
\vec{f}	Body force
f	Delay coefficient
\dot{f}_{vs}	Spray vapor mass flux at droplet surface
F	Force measured by dynamometer
F_{ib}, F_{ivm}	Virtual forces acted on i th spray element
F_{idr}	Drag force acted on i th spray element
F_{ig}	Gravitational force acted on i th spray element
F_{ip}	Pressure force acted on i th spray element
g	Gravity
h	Enthalpy
h_{evap}	Evaporation enthalpy
h_{fr}	Enthalpy of fresh gas

h_{gs}	Enthalpy of gas at droplet surface
h_s	Enthalpy at droplet surface
h_{sv}	Vapor enthalpy at droplet surface
h_∞	Enthalpy at particle far-field
k	Turbulent kinetic energy, conduction heat transfer coefficient, isentropic exponent and reaction rate
k_{xb}	Backward constant of the x th reaction
k_{xf}	Forward reaction rate constant of the x th reaction
K_{eff}	Mean stretch rate of the flame
K_t	Turbulent flame stretch
l	Connecting rod length
L	Piston displacement length and latent heat of evaporation
Le	Lewis number
\dot{m}_a	Mass flow rate of air
m_d	Mass of droplet
m_{fg}	Mass of gaseous fuel
m_o	Mass of oxidized soot
m_s	Mass of soot particles
m_{sf}	Mass of formed soot
\dot{m}_f	Mass flow rate of fuel
M_k	Molar mass of species k
n_m	Mechanical efficiency
n_{cyc}	Number of cycle
N	Engine speed
N_x	Molar concentration of the species x
$N_{O_x}^{u,M} _{u,M}$	Molar concentration of oxidizer in unburned, mixed zone
$N_{F_u}^{u,M} _{u,M}$	Molar concentration of fuel in unburned, mixed zone
p	Pressure
p_c	In-cylinder pressure
p_{ref}	Reference pressure
p_x	Partial pressure of component x

p_0	Initial pressure
P	Power
P_{CS}	Crankcase scavenging power
P_{fr}	Friction power
P_{MC}	Power mechanically charged devices
P_{SP}	Scavenging pump power
\dot{q}_s	Heat release rate from droplet surface
\dot{Q}	Heat release rate
r	Droplet radius
r_c	Compression ratio
r_{stable}	Radius of product droplet
\dot{r}	Fuel consumption rate
\dot{r}_k	Reaction rate of species k
R	Universal gas constant
R_0	Initial gas constant
\dot{r}_{fu}	Reaction rate of fuel
S	Stoichiometric oxygen requirement
S_a	Annihilation of flame surface
Sc	Schmidt number
Sc_t	Turbulent Schmidt number
S_{evap}	Evaporation source term
S_g	Production of the flame surface by turbulent rate of strain
S_L	Laminar flame speed
S_{LAM}	Laminar component of flame surface density
S_{PROP}	Propagating flame surface density
S_{CURV}	Curvature flame surface density
S_{STR}	Straining flame surface density
S_{y_k}	Mass source term of species k
S_Σ	Turbulent flame surface speed
S_{L0}	Initial laminar flame speed
T	Torque and temperature

T_d	Temperature of droplet
T_0	Initial temperature
T_{fr}	Fresh gas temperature
T_{max}	Maximum temperature
T_{min}	Minimum temperature
T_{ref}	Reference temperature
u_d	Absolute velocity of droplet
u_g	Absolute velocity of gas
u_{rel}	Relative velocity of droplet
$v_{i,r}$	Stoichiometric coefficients of species i in reaction r
V_p	Particle volume
V_c	Cylinder clearance volume
V_d	Piston displacement volume
w_L	Mean laminar fuel consumption rate
$w_{fu,x}$	Laminar fuel consumption rate for the x th reaction
w_s	Angular velocity of swirl
y_{EGR}	EGR mass fraction
y_{fu}	Fuel mass fraction
$y_{fu,fr}$	Fuel mass fraction in the fresh gas
y_k	Mass fraction of species k
\bar{y}_k	Ensemble-averaged mass fraction of species k
\tilde{y}_k	Density weighted ensemble-averaged mass fraction of species k
y_{O_x}	Fuel oxidizer mass fraction
$y_{O_2,fr}$	Oxygen mass fraction in fresh air
y_{Pr}	Combustion product mass fraction
y_{vs}	Mass fraction of vapor at droplet surface
$y_{v\infty}$	Mass fraction of vapor at particle far-field
y_k^*	Local instantaneous mass fraction of species m
α	CFM correction constant
α_{cnv}	Convective heat transfer coefficient

α_{fu}	Stoichiometric function of fuel
β	CFM constant and binary diffusion coefficient
γ	Reaction rate multiplier
ε	Disipation rate
λ	Air excess ratio
μ	Dynamic viscosity
μ_{eff}	Effective dynamic viscosity
μ_t	Turbulent dynamic viscosity
ν_t	Turbulent kinematic viscosity
ρ	Density
ρ_d	Liquid droplet density
ρ_g	Mixed gas density
ρ_{fr}	Density of the fresh gas
σ	Surface tension
σ_e	Turbulence model constant
σ_k	Turbulence model constant
σ_p	Turbulence model constant
σ_Σ	Turbulent Schmidt number
Σ	Turbulent flame surface density
τ_a	Break-up time scale
τ_c	Characteristic time scale
τ_d	Ignition delay time scale
τ_l	Laminar time scale
τ_R	turbulent mixing time scale
τ_t	Turbulent time scale
ϕ	Equivalence ratio and thermal source term
ϕ_{fr}	Richness of fresh gas
ϕ_{crit}	Critical equivalence ratio

LIST OF ACRONYMS/ABBREVIATIONS

1D	One Dimensional
2D	Two Dimensional
2DS	The 2°C Scenario
3D	Three Dimensional
AMEP	Auxiliary Drives Mean Effective Pressure
A/F	Air-Fuel Ratio
aTDC	After Top Dead Center
BC	Bottom Dead Center
BDC	Bottom Dead Center
BMEP	Break Mean Effective Pressure
bTDC	Before Top Dead Center
CFD	Computational Fluid Dynamics
CI	Compression Ignition
CR	Compression Ratio
DFP	Diesel Particulate Filter
ECFM	Extended Coherent Flame Model
ECFM-3Z	Extended Coherent Flame Model Three-Zone
EGR	Exhaust Gas Recirculation
EPA	Environmental Protection Agency
FMEP	Friction Mean Effective Pressure
F/A	Fuel-Air Ratio
GDICI	Gasoline Direct Injection Compression Ignition
GHC	Green House Gases
HC	Hydrocarbon
HCCI	Homogeneous-Charge Compression Ignition
HSDI	High Speed Direct Injection
ICE	Internal Combustion Engine
IMEP	Indicated Mean Effective Pressure

LII	Laser Induced Incandescence
LTC	Low Temperature Combustion
MEP	Mean Effective Pressure
PCCI	Premixed Charge Compression
PDA	Phase Doppler Anemometry
PFP	Peak Firing Pressure
PIV	Particle Image Velocimetry
PLIF	Planer Laser Induced Fluorescence
PM	Particulate Matter
RCCI	Reactivity Controlled Compression Ignition
rpm	Round Per Minute
SCR	Selective Catalytic Reduction
SI	Spark Ignition
SMD	Sauter Mean Diameter
SOC	Start of Combustion
SOI	Start of Ignition
SR	Swirl Ratio
TC	Top Dead Center
TDC	Top Dead Center

1. INTRODUCTION

Nowadays, our society relies heavily on internal combustion (IC) engines for transportation, commerce and power generation. Due to this dependence, engine research activity has lasted more than a century-long time and it is still vibrant today. The internal combustion engines, reciprocating engines in particular, vary in size from model airplane engines fitting in the hand, to enormous marine engines and they power numerous devices such as pumps, chain-saws, tractors, propeller aircraft, ships etcetera. 90.6 million motor vehicles were produced in 2014, of which well over 72.3 million were passenger cars [1]. Figure 1.1 summarizes the world's motor vehicle production between 2000 and 2014. The world's largest car manufacturer is China producing a quarter of world's cars while a third of all cars are manufactured in European Union. Roughly half of those cars are diesel-powered due to their superior efficiencies, so today engine researches comprises both gasoline and diesel engines. As it can be understood by the volume of the use of IC engines, even a small improvement in their efficiency has a great impact on economy and pollution.

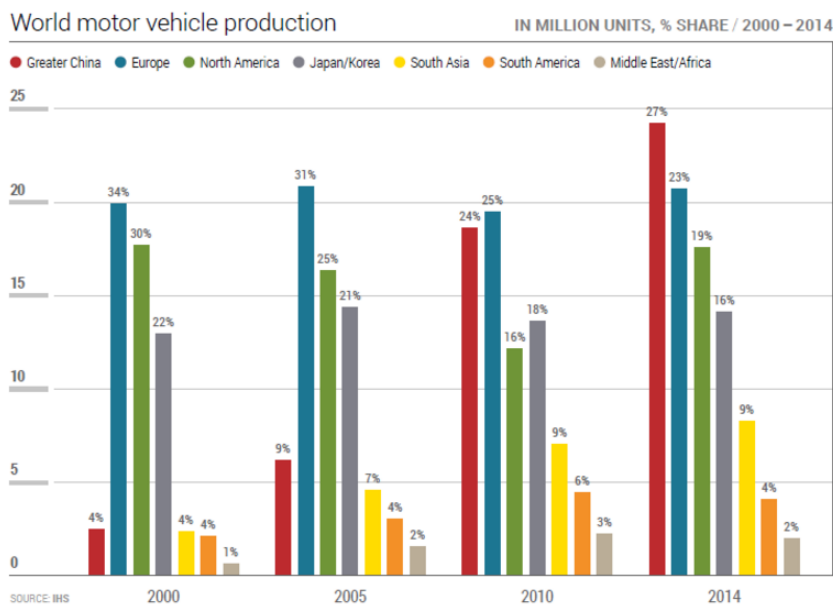


Figure 1.1. World motor vehicle production [1].

The large number of vehicles in the world use an enormous amount of fuel to extract the needed energy. The massive use of fuel leads to undesired emissions such as nitric oxide (NO_x), particulate (soot), hydrocarbons, CO and CO₂ which may cause serious environmental and health problems, thus a number of stringent vehicle emission regulations have been imposed by most governments and these regulations have constantly been tightened further over time. The world's yearly production of 37 million tons of CO₂ leads to Green House Gases (GHG), which may cause climate changes with adverse results. In addition, International Energy Agency accordingly aims at reducing the use of fuel per kilometer by 30-50 % in new road vehicles worldwide by 2030 then in all vehicles in the world by 2050 [9]. The purpose is to restrict the global average temperature rise according to the 2DS scenario of some climatologists [10]. All these environmental and health-related concerns have given birth to the need for internal combustion engine researches over a range of areas.

Despite all these handicaps, gasoline and diesel fuels are chiefly used worldwide. The reason is because they are very compact and portable form of energy, producing over 40MJ of energy from a kg of fuel. Thinking that the kinetic energy of a car weighing a ton and travelling with 96 km/h can be obtained from roughly 30 ml of fuel, the demand on the use of fuel becomes apparent. The huge amount of energy extracted from the fuel comes from the sequential chemical reactions in which hydrocarbon bonds are broken with O₂ while CO₂ and H₂O are produced. However, most of the extracted energy cannot be harnessed due to internal and external losses. When 100 % of pure energy in fuel enters the gas tank of the vehicle, a typical Spark-Ignition (SI) engine delivers roughly 18 % of energy to its wheels. The losses are mainly 62 % for engine and exhaust losses, 20 % for running accessories and stand-by-idle losses and the losses from the driveline [10]. Figure 1.2 shows overall energy losses in a typical gasoline engine passenger car [2].

Researches and experiments on internal combustion engines have enjoyed over century-long background. Nowadays these studies are mostly on the understanding of the combustion process and reducing the undesired emissions to promote more efficient and environmentally friendly engines with tolerable emissions. Thanks to the

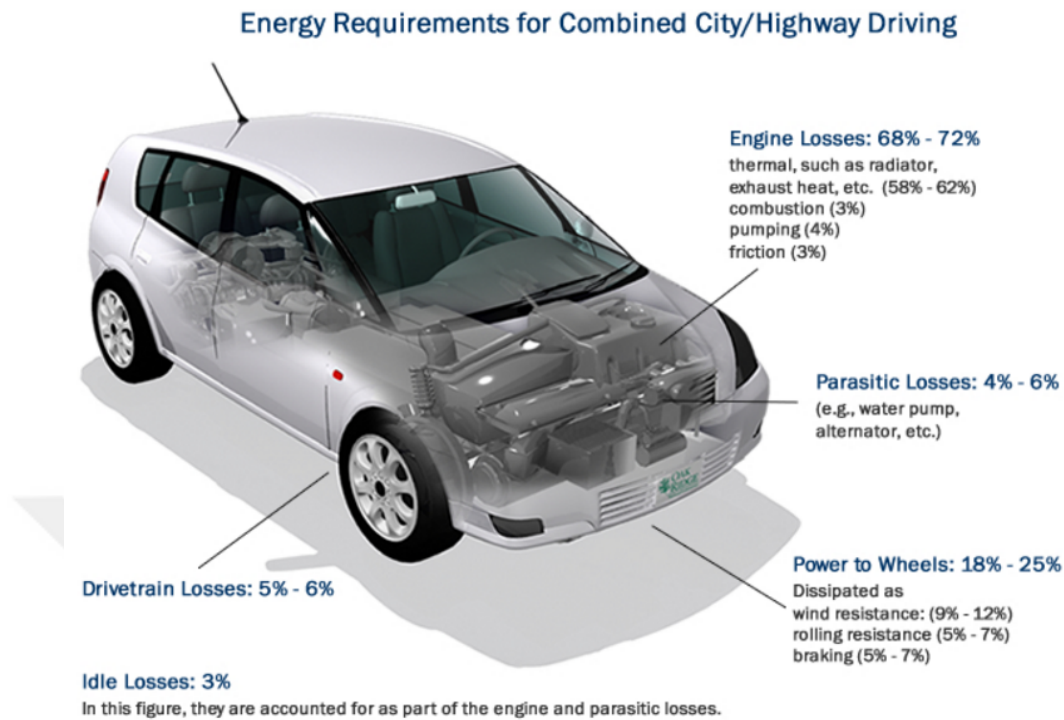


Figure 1.2. Energy losses for gasoline vehicles [2].

power of computers, comprehensive computer codes are now widely used in engine research rather than describing the engine process with empirical ways as in conventional thermodynamically-based analyses. The governing differential equations of Navier Stokes can be solved numerically via computers.

The novelty of the combustion process has led to a countless number of discoveries for decades. Engine combustion process can be considered as a low Mach number, compressible, multi-phase, high-Reynolds number turbulent flow with chemical reactions accompanied with heat transfer within a time-varying geometry. Due to its being quite challenging, Computational Fluid Dynamics (CFD) models have been developed. It has become more possible to deal with such complexities and to design more efficient and cleaner IC engines. The improvement of more accurate CFD models aids the development of new Low temperature Combustion (LTC) concepts. LTC engine has a higher efficiency and it is cleaner than its counterparts because low temperature operation causes lower thermal losses through the cylinder walls and reduction in NOx

emissions because of the high activation energy of NO formation reactions. [9] LTC concepts can be classified as Homogeneous Charge Compression Ignition (HCCI), Premixed Charge Compression Ignition (PCCI) and Reactivity Controlled Compression Ignition (RCCI).

Development of Computational Fluid Dynamic (CFD) tools has paced the engine researches. A number of open-source and commercial packed programs have emerged for decades. RICE, CONCHAS-SPRAY, KIVA, KIVA-II, KIVA-3V, KIVA-4 and OpenFOAM as open source codes and STAR-CD, AVL FIRE, Ricardo VECTIS, FLUENT, CONVERGE and FORTE as commercial codes have been promoted from 1970's up to present. These CFD codes have some advantages and disadvantages over one another for corresponding models and sub-models. For example, The KIVA code is chiefly used for spray combustion modeling due to its being open-source code in particular for academic researches. However, even the latest version of it-KIVA3V- has limited ability to model complex geometries. On the other hand, other commercial codes like FIRE, STAR CD, FLUENT, VECTIS, which are mainly for industrial purposes, are able to model quite complex geometries and they are user friendly programs.

Engine experiments which are critical to provide insights into combustion processes greatly help CFD model development process. For instance, Planer Laser Induced Fluorescence or Incandescence (PLIF and LII), chemical luminescence and soot thermal emission give detailed data about in-cylinder spatial and temporal distributions of important species. For spray drop size and velocity analysis, Particle Image Velocimetry(PIV) or Phase Doppler Anemometry(PDA) provide beneficial information. Furthermore, some out-of-engine experiments such as shock tube, rapid compression experiments provide information about ignition characteristics of fuel. Constant volume combustion vessel experiments are used for information about spray vaporization, fuel-air mixing, spray ignition, flame lift-off and fuel effects on particulate (soot) formation and oxidation. Flame measurements also provide helpful data for the development of flame propagation models.

In conclusion, internal combustion engines are widely employed today for various purposes. The Spark-Ignition (SI) engine is the least efficient partly due to high flame temperatures which contribute to high wall heat transfer rates and to increase in NO_x emissions. The conventional diesel engine has 20-40 % more fuel efficiency than the SI engine. Relatively high compression ratio and lack of throttling losses elevate the efficiency of diesel engines. If high Exhaust Gas Recirculation (EGR) rates are not used, local temperatures in the chamber increase and it leads to high NO_x emissions. In addition, due to the stratified charge, high soot emissions are produced by fuel rich regions. So providing both thermal efficiency and clean combustion has become a deal and it has led to the need for the development of costly exhaust gas after-treatment systems. Advanced combustions concepts like Gasoline Direct Injection Compression Ignition (GDICI) and RCCI are 20% more fuel efficient than standard diesel concepts and 40-50% more fuel efficient than SI engines. RCCI engine has another advantage of fuel flexibility. It can be powered by gasoline, natural gas, diesel plus some alternative and renewable fuels such as hydrated ethanol, methanol and biodiesel. It is obvious that the IC engines are remarkably efficient and when integrated with the technologies which provide fuel flexibility, it paves the way out of the fossil fuel monopoly for the security of our future energy.

2. INTERNAL COMBUSTION ENGINES

2.1. Engine Operating Cycles

Internal combustion engines, in particular SI and CI engines, are complex machines which produce work by reciprocating motion of a piston through a cylinder. The reciprocating motion of a piston is transferred into the rotary motion by a crank shaft. The elevated pressure achieved in the cylinder due to the fuel oxidation pushes the piston down and gives a rotation to the crank shaft. As it is shown in the Figure 2.1, the piston shuttles between the top dead center (TDC or TC) and the bottom dead center (BDC or BC) during the entire process. There is a number of types of ICEs such as two-stroke and four-stroke SI engines or CI diesel engines. In the present work, four-stroke CI diesel engine has been considered. Within the four-stroke, intake stroke where air is introduced into the cylinder as the piston moves from TDC to BDC is the first phase. Then compression stroke, where piston compresses the air by moving from BDC to TDC, occurs. The third stroke, expansion stroke, combustion takes place when the injector injects fuel into the cylinder around the TDC then power is generated as the piston moves to the BDC. This process is also called power-stroke. The final stroke, exhaust stroke, occurs as piston moves from the BDC to the TDC where burned gasses exit the cylinder.

2.2. Engine Design and Operating Parameters

There is a variety of terms used to describe the geometry and the operational characteristics of an engine. As it is shown in the Figure 2.2, a couple of dimensions like bore diameter(B), stroke length(L), connecting rod length(l) and so on are needed to describe a specific engine. In the figure, V_d represents the displacement volume swept by the cylinder as V_c means the clearance volume on the top of the cylinder which is the space between cylinder head and the piston head when pistons arrives at the TDC. Some of the important parameters are described in the following sections.

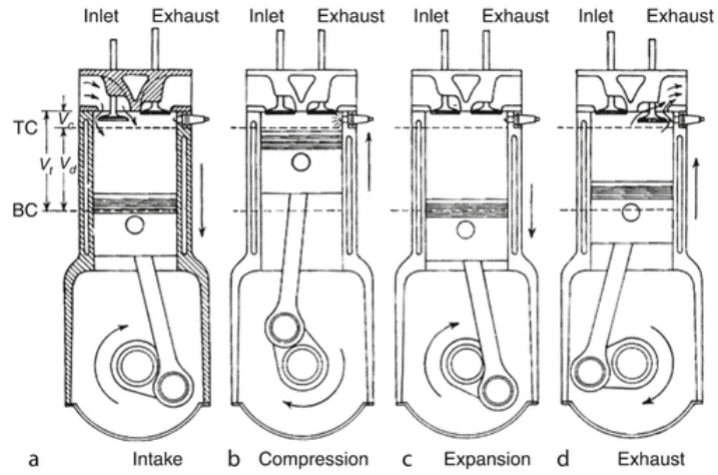


Figure 2.1. The four-stroke operating cycle [3].

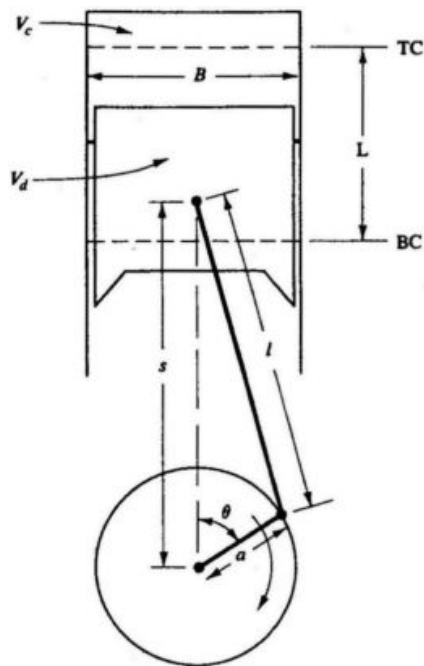


Figure 2.2. Geometry of cylinder and piston [3].

2.2.1. Compression Ratio

Compression ratio r_c is one of the most important geometrical parameter for an ICE. This is basically the ratio of maximum volume to minimum volume in the cylinder during operation and formulated as:

$$r_c = \frac{V_d + V_c}{V_c} \quad (2.1)$$

The compression ratio is limited in SI engines since those engine compresses air-fuel mixture thus it is not possible to exceed a threshold at which the ignition temperature is reached. However, in CI diesel engines, maximum available compression ratio value is higher since these engines compress only air, which eliminates an unexpected ignition, during the compression stroke. The typical compression ratios r_c are 8 to 12 for SI engines and 12-24 for CI engines [3].

2.2.2. Brake Torque and Power

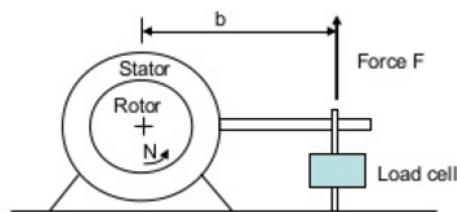


Figure 2.3. Schematic of principle of operation of dynamometer.

Engine torque T is measured by a dynamometer attached to an engine as shown in Figure 2.3. The torque is the basically calculated as:

$$T = Fb \quad (2.2)$$

Then the power can be calculated as the product of engine speed(N) and measured torque(T) as follow:

$$P = 2\pi NT \quad (2.3)$$

Torque means the ability of an engine to do work and the power means the rate at which work is done.

2.2.3. Mean Effective Pressure

2.2.3.1. Indicated Mean Effective Pressure. Indicated Mean Effective Pressure(IMEP) is the fictitious pressure value calculated via dividing work done per cycle by the total displacement volume. Since the area under the pressure curve in a pressure-volume plot gives the work done by the engine, the following expression is used to define IMEP:

$$IMEP = \frac{1}{V_d} \oint p_c dV \quad (2.4)$$

2.2.3.2. Friction Mean Effective Pressure. FMEP is derived from the frictional forces due to the friction between moving parts like piston-cylinder and piston liner-cylinder and calculated by:

$$FMEP = \frac{P_{fr}}{V_d n_{cycle}} \quad (2.5)$$

where P_{fr} is called friction power and n_{cycle} is calculated for four-stroke engines as:

$$n_{cycle} = \frac{N}{2} \quad (2.6)$$

where N is crankshaft-revolutions per second(Engine speed).

2.2.3.3. Auxiliary Drives Mean Effective Pressure. AMEP arises from the power losses in scavenging pumps, crankcase scavenging or mechanically driven supercharging devices and it is defined as:

$$AMEP = \frac{P_{SP} + P_{CS} + P_{MC}}{V_d n_{cycle}} \quad (2.7)$$

where P_{SP} , P_{CS} and P_{MC} represents, in order, required power for scavenging pumps, crankcase scavenging and mechanically driven supercharging devices.

2.2.3.4. Break Mean Effective Pressure. BMEP is a fictitious pressure calculated by subtracting FMEP and AMEP from IMEP as follows:

$$BMEP = IMEP - FMEP - AMEP \quad (2.8)$$

Note that mechanical efficiency n_m gives the correlation between IMEP and BMEP as:

$$n_m = \frac{BMEP}{IMEP} \quad (2.9)$$

2.2.4. Air-Fuel and Fuel-Air Ratios

A/F and similarly F/A ratios are calculated by dividing the mass of air by the mass of fuel in the cylinder or vice versa as follows:

$$A/F = \frac{\dot{m}_a}{\dot{m}_f} \quad (2.10)$$

$$F/A = \frac{\dot{m}_f}{\dot{m}_a} \quad (2.11)$$

Typical A/F ratio ranges from 12 to 18 for a conventional SI engine and it is between 18 and 70 for CI diesel engines [3].

2.2.5. Excess Air Ratio

Excess air ratio, denoted by λ , is a measure of how excess air is with respect to amount of air in stoichiometric condition and expressed by:

$$\lambda = \frac{(A/F)_{Cmb}}{(A/F)_{Stc}} \quad (2.12)$$

2.2.6. Equivalence Ratio

Equivalence ratio, denoted by ϕ , is a measure of how excess fuel is with respect to amount of fuel in stoichiometric condition and expressed by:

$$\phi = \frac{(F/A)_{Cmb}}{(F/A)_{Stc}} = \frac{1}{\lambda} \quad (2.13)$$

2.2.7. Swirl Ratio

Swirl is the rotational charge motion about the cylinder axis intentionally created by bringing the intake flow with an initial angular momentum in order to promote more rapid air-fuel mixing in the cylinder. Used to speed up the combustion process, swirl is also used in two-stroke engines for better scavenging. The term swirl ratio SR can be calculated by dividing the angular velocity of a solid-body rotating flow by the angular rotational speed of the engine as follows:

$$SR = \frac{w_s}{2\pi N} \quad (2.14)$$

where w_s is the angular velocity of the swirl and N is the engine speed(rpm).

3. STUDIES IN THE LITERATURE

Traditional compression ignition diesel engine combustion is characterized by high NO_x and soot emissions due to the varying local equivalence ratios and temperatures of the combustion spray in the cylinder. Exhaust Gas Recirculation (EGR) which recycles and reintroduces exhaust gas into the combustion chamber system is used to reduce NO_x emissions by lowering the combustion chamber temperature and available oxygen in the cylinder. Selective Catalytic Reduction (SCR) exhaust gas after treatment system has been preferred by most diesel engine manufacturers to reduce NO_x emissions. Soot control can be achieved by using Diesel Particulate Filters (DPF). However, these exhaust gas after treatment systems are not cost efficient because of the need for fuel penalties (1 % for SCR and 2-4 % for DPF per 1g/kW [10]) emission reduction which makes them as expensive as the engine itself. But still, the effectiveness of modern after treatment systems is significant.

It is prevalent that direct injected (DI) diesel engines have been used widely as a power source due to their superior efficiencies. However, main problem arises from the emission rates (NO_x and PM (particulate matter)). Legislative laws are becoming continuously stricter on emissions rate by reducing them to extremely low values. One proper way to reduce NO_x emission is the use of higher exhaust gas recirculation (EGR) rates with increased boost pressure to prevent negative impact of EGR on soot emissions. A typical EGR system integrated into a diesel engine has been shown in Figure 3.1. The principle of EGR method to reduce NO_x emission is lowering available O₂ and the overall temperature inside the combustion chamber but it has negative effect on soot emissions and brake specific fuel consumption (bsfc). To overcome these adverse effects, it is necessary to use EGR gas cooling system. Because of that, in D.T. Hountalas et al. [11] study, 3D multi-zone combustion model has been used to examine the effect of various EGR rates and temperature on performance and emissions of a turbocharged DI diesel engine. The study comprises engine cylinder (heat transfer, air swirl, spray model, air entrainment into the zones, droplet break-up and evaporation, combustion model) simulation and nitric oxide and soot formation simulations which

are validated by an experiment conducted at DaimlerChrysler laboratory. It has been found that the use of high EGR temperature (lower cooling) has a negative impact on brake engine efficiency, peak combustion pressure, soot emissions and air-fuel ratio (A/F). As a result, it has been asserted that the result of low EGR temperature is stronger than high EGR rates and EGR cooling is favorable to prevent soot emissions from rising to unacceptable levels and to retain the benefits of low NO_x emissions without worsening the engine efficiency.

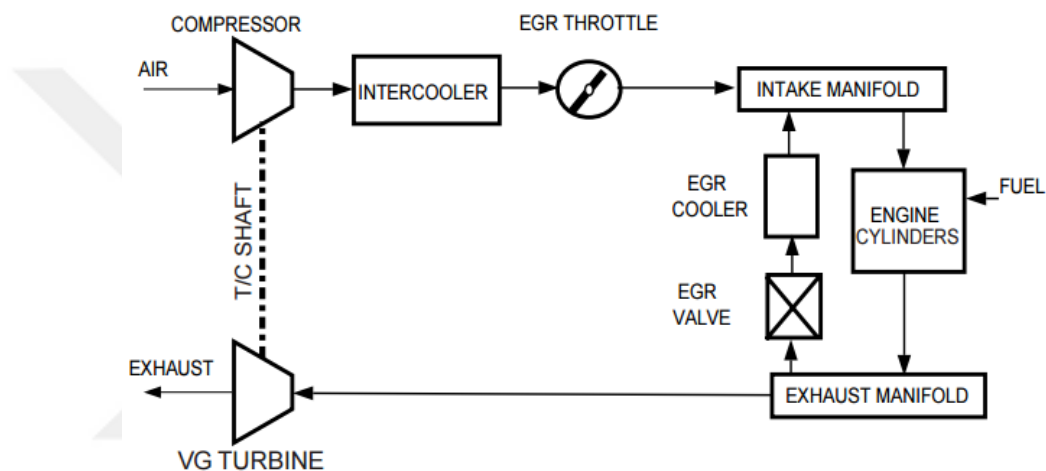


Figure 3.1. EGR system [4].

In Dong Wang's and Chao Wang's study [12], a prediction model which reveals a linear relation between the nitrogen oxides (NO_x) emissions and the in-cylinder heat release rate in DI diesel engine has been developed. A modified KIVA-3V code has been employed to calculate NO_x formation and heat release rate in the combustion chamber. The governing equations for the model are basically continuity, momentum, energy, gas state, standard $k-\epsilon$ turbulence equation and extended Zeldovich mechanism. The result shows that the NO_x formation depended on both the magnitude and timing of the peak heat release rate in each cycle. In a small scale diesel engine, a dynamic NO_x model has been established and then applied into a feedback emission control system. A new parameter, combustion acceleration has been defined to refer the intensity of the premixed combustion. To measure real time in-cylinder pressure at each crank angle and the heat release rate, an experimental work has been conducted. The overall

study shows that the proposed NOx prediction model is useful to control NOx emissions under high engine speeds.

Another study conducted by Shengli Wei et al. [13] puts the effect of swirl ratio on DI diesel engine system into consideration. By using the AVL Fire code, the mixture formation and combustion progress in the cylinder are simulated with various swirl ratios. In the simulation, $k-\epsilon$ turbulence model, WAVE breakup spray model, Dukowicz evaporation model, walljet1 wall interaction model, extended Zeldovich for NO model and Kennedy-Hiroyasu-Magnussen soot model are employed. For the model verification, the result of in cylinder pressure and heat release rates are compared with experimental data. The result reveals that the uniformity of the mixture is better with swirl ratio of 0.2 while NO mass fraction is the highest at SR 2.7 and the lowest at SR 0.8. Furthermore, SR 0.2 leads to the highest soot formation and SR 3.2 leads the lowest. In conclusion, swirl ratio of 0.8 is the best for emissions.

Various scientific studies have been made on DI diesel engines for better understanding of their complications and subtle processes. A 3D simulation study conducted by R. Tatschl and P. Priesching [14] focused on CFD model of DI diesel engine combustion and pollutant formation to analyze and assess the sensitivity of the adopted combustion and emission modeling approaches. Coherent flame modeling approach has been employed for premixed flame and diffusion combustion. Equilibrium chemistry approach and three step mechanism have been used for high temperature oxidation while Zeldovich and reduced chemical kinetics soot model have been employed for NOx and soot emissions. CFD code AVL FIRE have been used to examine the influence of various in-cylinder swirl, start-of-injection, injection pressure and residual gas content on the engine combustion and emissions. Fuel spray propagation has been modeled in accordance with Lagrangian discrete droplet method. Ignition and combustion processes have been modeled with ECFM-3Z. The result of the study reveals that the comparison between measured and calculated results shows good match for both the in-cylinder pressure traces and pollutant emissions while calculated heat release rates show some slight deviation from the measured ones.

In V. Rao's and D. Honnery's study [15], a comparison between two NOx models coupled to a multizone quasi-dimensional diesel engine model to obtain NOx predictions for diesel fuel in a DI naturally aspirated diesel engine has been made. Spray evolution, fuel evaporation, air entrainment, ignition delay, ignition, combustion and product formation have been modeled accordingly, and then Mellor and extended Zeldovich NOx sub-models have been employed. With experimental results, predictions of cylinder pressure, heat release and NOx emissions have been verified. Over a range of engine loads and speed, the model predicted cylinder pressure and heat release with good accuracy. The Mellor NOx model [16] has shown better performance than Zeldovich model when the same calibrations have been used. However, the extended Zeldovich model gives good predictions when empirical constants were modified to fortify NOx prediction at specific engine condition. To sum up, The Mellor model has been found to provide superior performance over a range of engine conditions.

In the study of C.D. Rakopoulos et al. [17] an investigation has been made to compare the simulation results of a high speed direct injection(HSDI) diesel engine with three different piston bowl geometry and three rotational speeds ($d/D=64\%$ (standard case), 54% , 44% and 1500rpm , 2000rpm , 2500rpm) by employing two recent diesel engine simulation models -CFD model and detailed quasi-dimensional model- developed by the authors. The CFD code can simulate 3D curvilinear domains with finite volume approach in a collocated grid and it solves the transport equations for momentum-energy-mass conservation coupling with $k-\varepsilon$ turbulence model and some modification to introduce the compressibility of a fluid. The quasi-dimensional model solves general transport equation for conservation of mass and energy with finite volume approach within the entire in-cylinder, while a new simplified three dimensional air motion model is used to estimate the flow field. For comparison of these two models, the in-cylinder spatial and temporal temperature distribution, the mean cylinder pressure diagram, the mean in-cylinder radial and axial velocity are determined. For all cases examined, both models provide similar prediction of in-cylinder temperature distributions and mean air velocity fields at each crank angle. Thus, the quasi-dimensional model with proposed simplified air motion is shown to be more time efficient than more detailed and accurate CFD model and it is able to capture the physical effect of combustion

chamber geometry and the speed on the in-cylinder velocity and temperature field. The CFD model is more appropriate for the detailed simulations which involves in-cylinder geometry complications. The authors aim at further improving the quasi-dimensional model by integrating a turbulence model and more sophisticated wall heat transfer formulations.

A computational investigation of the effects of swirl ratio and injection pressure on wall heat transfer in light-duty engine has been made by Rolf D. Reitz et al. [7] by using KIVA3V-ERC code. Experimental results which involves a planar laser-induced fluorescence(PLIF) methodology to get local mixture equivalence ratio values based on a diesel fuel surrogate (75 % n-heptane, 25 % iso-octane) plus a small fraction of toluene as fluorescing tracer(0.5 % in mass) are used to validate the CFD model. The purpose of the study is to further validate engine CFD simulations and to better understand the role of wall heat transfer on combustion with high injection pressures and swirl ratios. Swirl ratios ranges from 1.55 to 4.50, injection pressure ranges from 500 bar to 1220 bar. The study shows that higher swirl ratios lead to significant increase in wall heat transfer with slight delays in predicted ignition timing. Furthermore, the injection pressure has a major role on the combustion development. Elevated injection pressures cause to increase in wall heat transfer and it also leads to delay in ignition timing. Also the model shows that greater penetration into the squish region and crevice volume may lead to misfiring conditions. To sum up, the CFD model proved to be a reliable and convenient way to simulate low-load and low-temperature combustion in light-duty engine.

4. MATHEMATICAL APPROACH TO ICE MODELING

ICE combustion modeling requires a variety of complex mechanisms such as turbulence, spray-charge dispersion and their interactions, subsequent chemical reactions to take into account. In the literature, there are a number of models and submodels corresponding to each important participating phenomenon. A good understanding and implementation of spray propagation, break-up, turbulent mixing, interaction between each species and chemical reaction is key to a successful combustion simulation reflecting realistic results. Basically, three conservation equations, namely for mass, momentum and energy are to be solved together with species transport equations within the domain divided into a finite number of cells, so-called meshes. For this particular study, the domain- the region to be meshed-is the inside of the cylinder where all combustion process takes place. Figure 4.1 shows a typical discretization of a domain where all process occurs in the cylinder.

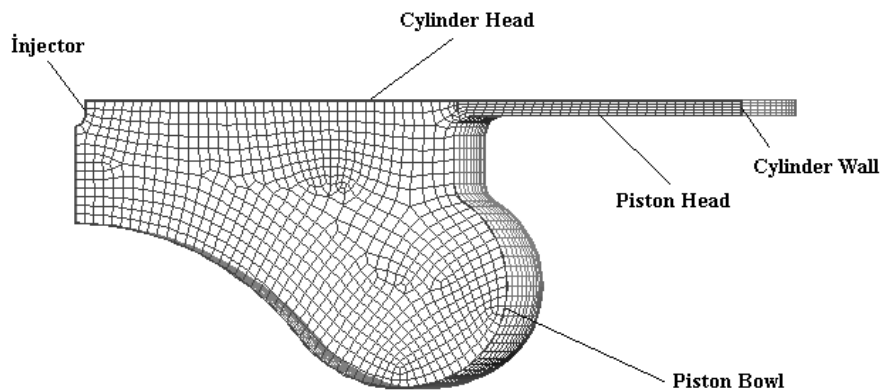


Figure 4.1. Example of a discretization for in-cylinder.

The border of this domain is determined by the geometry of injector, cylinder head-wall, piston head-wall and piston bowl. The governing equations for mass species transport is given below:

$$\frac{\partial}{\partial t}(\rho y_k) + \frac{\partial}{\partial x_i}(\rho(u_i - u_{\delta i})y_k) = \frac{\partial}{\partial x_i}\left(\Gamma_{y_k} \frac{\partial y_k}{\partial x_i}\right) + S_{y_k} \quad (4.1)$$

$$\Gamma_{y_k} = \left(\rho D_{k,m} + \frac{\mu_t}{Sc_t}\right) \quad (4.2)$$

$$S_{y_k} = \dot{r}_k M_k \quad (4.3)$$

where y_k represents the mass fraction of an individual species k , Sc_t is the turbulent Schmidt number, $D_{k,m}$ is the diffusion coefficient of species k . In the formula for mass source, S_{y_k} , calculation, \dot{r}_k and M_k stand for reaction rate and molar mass of species k , respectively. The momentum and energy conservation equations are expressed as follows:

$$\rho \frac{\partial u_i}{\partial t} + \rho u_j \frac{\partial u_j}{\partial x_j} = \rho g_i - \frac{\partial p}{\partial x_i} + \frac{\partial}{\partial x_j} \left[\mu \left(\frac{\partial u_i}{\partial x_j} \frac{\partial u_j}{\partial x_i} - \frac{2}{3} \frac{\partial u_k}{\partial x_k} \delta_{ij} \right) \right] \quad (4.4)$$

$$\rho \left(\frac{\partial h}{\partial t} + u_j \frac{\partial h}{\partial x_j} \right) = \rho \dot{q} + \frac{\partial p}{\partial t} + \frac{\partial(\tau_{ij} u_j)}{\partial x_i} + \frac{\partial}{\partial x_j} \left(\lambda \frac{\partial T}{\partial x_j} \right) \quad (4.5)$$

Note that turbulence model equations will be covered in Section 4.3.4.

4.1. Combustion Models

Combustion process in CI engines commences with auto-ignition, when sufficient temperature and pressure reached during the compression stroke after injection of fuel. There are four phases of combustion in diesel engine, those are namely, in order, ignition delay period, premixed combustion, mixing-controlled combustion or diffusion

combustion and late combustion phase as shown in the Figure 4.2. Combustion process does not start right after injection commences. There is a time interval between the start of injection SOI and start of combustion SOC, where proper conditions are formed in the cylinder for the combustion. This period is called as ignition delay time. After this delay period, the premixed combustion phase, where most of the fuel injected is burned, begins. After the premixed combustion at which elevated heat release rates are observed, the mixing-controlled combustion phase begins and it is followed by the last phase the late combustion.

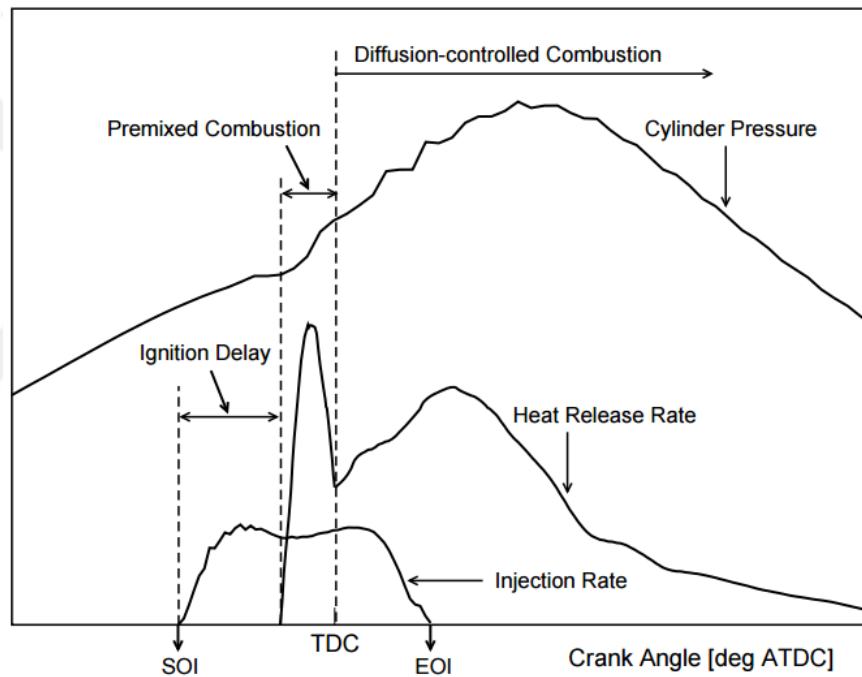


Figure 4.2. Conventional diesel engine combustion stages [5].

The following sections describe some of prevailing combustion models in the literature developed for simulation of species transport, turbulent combustion of gaseous mixture of hydrocarbon fuel-air and residual gas. These combustion models, namely Eddy Break-up, Characteristic Timescale and Coherent Flame Model, are to be elaborated together with their theoretical definitions, assumptions and mathematical formulations.

4.1.1. Eddy Break-Up Model

Described by Magnussen and Hjertager [18], Eddy Break-Up model is a turbulent mixing-controlled type model. In this model, rate of combustion is determined by the rate of dissipation of the eddies (reactants and hot products) since the chemical reactions mostly have very short time scales compared to the characteristics of the turbulent combustion process. The appealing feature of this model is that it does not require the predictions of fluctuations of reacting species. In the model, mean reaction rate can be written accordingly as follows:

$$\overline{\rho \dot{r}_{fu}} = \frac{C_{fu}}{\tau_R} \bar{\rho} \min \left(\bar{y}_{fu}, \frac{\bar{y}_{Ox}}{S}, \frac{C_{Pr} \bar{y}_{Pr}}{1+S} \right) \quad (4.6)$$

In the right-hand side of the equation, the first two arguments of the minimum value operator ($\min(\dots)$) determine whether fuel or oxygen is present in limiting amount, and the third argument is called reaction probability which makes sure that in the lack of hot reactants, the flame is not propagated. C_{fu} and C_{Pr} are empirical constants as τ_R stands for the turbulent mixing time scale for reaction. C_{fu} value has to be determined in accordance with the experimental combustion data for each specific case.

4.1.2. Characteristic Timescale Model

Mixing-controlled phase is considered as an integral part of combustion in diesel engines. Thus, turbulence-chemical reaction interactions have to be put into consideration. This model consolidates a laminar and a turbulent time scale to a general reaction rate [19]. The following equation represents the time rate of change of a species k with respect to this time scale:

$$\frac{dy_k}{dt} = -\frac{y_k - y_k^*}{\tau_c} \quad (4.7)$$

where y_k means the mass fraction of the species k and y_k^* is the local instantaneous thermodynamic equilibrium value of the mass fraction. τ_c in the denominator is the characteristic time for such equilibrium. To predict thermodynamic equilibrium temperature precisely enough, consideration of seven species of fuel, O₂, N₂, CO₂, CO, H₂ and H₂O is sufficient. Characteristic time scale can be written in terms of a laminar and turbulent time scale as follows:

$$\tau_c = \tau_l + f\tau_t \quad (4.8)$$

Laminar time scale τ_l and the turbulent time scale τ_t are derived as follows:

$$\tau_l = A^{-1}[C_x H_y]^{0.75}[O_2]^{-1.5} \exp\left(\frac{E_a}{RT}\right) \quad (4.9)$$

$$\tau_t = C_2 \frac{k}{\epsilon} \quad (4.10)$$

The increasing impact of turbulence on combustion after ignition is controlled by f and it is calculated with respect to the reaction progress r as follows:

$$f = \frac{1 - e^{-r}}{0.632} \quad (4.11)$$

$$r = \frac{y_{CO_2} + y_{H_2O} + y_{CO} + y_{H_2}}{1 - y_{N_2}} \quad (4.12)$$

The turbulent-mixing effects dominate the combustion within the range of $\tau_l \ll \tau_t$. In the region close to injector, the laminar time scale cannot be omitted since high velocities lead to a very small turbulent time scale in the region.

4.1.3. Coherent Flame Model

Coherent Flame Model (CFM) can be used for both premixed and non-premixed conditions within the scope of laminar flamelet concept in which mean values of velocity and thickness are only dependent on the pressure, temperature and the richness in fresh gases. Superior side of such model compared to others is that it takes both decoupled treatment of chemistry and turbulence into account. Since CFM is a kind of flamelet model, it assumes that reaction occurs within relatively thin layers which split the fresh unburned gas from fully burnt gas. The mean turbulent reaction rate can be calculated as the multiplication of the flame surface density Σ and the laminar burning velocity S_L as follows:

$$\overline{\rho \dot{r}_{fu}} = -w_L \Sigma \quad (4.13)$$

where w_L is the mean laminar fuel consumption rate per unit surface along the flame front as the following equation is used for lean combustion:

$$w_L = \rho_{fu,fr} S_L \quad (4.14)$$

where $\rho_{fu,fr} = \rho_{fr} y_{fu,fr}$, $\rho_{fu,fr}$ is the partial fuel density of the fresh gas and ρ_{fr} is the density of fresh gas.

The laminar flame speed S_L supposedly depends only on the local pressure, the fresh gas temperature T_{fr} , and the local unburned fuel/air equivalence ratio. The fresh gas temperature is computed in accordance with isentropic transformation formulation via:

$$T_{fr} = T_0 \left(\frac{p_0}{p} \right)^{\frac{1-k}{k}} \quad (4.15)$$

$$\rho_{fr} = \frac{p_0}{R_0 T_{fr}} \quad (4.16)$$

In the formula, R_0 is initial gas constant and k equals c_p/c_v at local conditions. Taking the correlation of Metghalchi et al. [20] into account, the following empirical expression, which is applicable for premixed combustion at high pressure and temperature, is obtained:

$$S_L = S_{L0}(1 - 2.1y_{EGR}) \left(\frac{T_{fr}}{T_{ref}} \right)^{a_1} \left(\frac{p}{p_{ref}} \right)^{a_2} \quad (4.17)$$

where T_{ref} and p_{ref} are the reference values for standard state, a_1 and a_2 are the fuel dependent parameters and y_{EGR} is the exhaust gas mass fraction. To compute the flame surface density, the following equation is used:

$$\frac{\partial \Sigma}{\partial t} + \frac{\partial}{\partial x_i} (\bar{u}_i \Sigma) - \frac{\partial}{\partial x_i} \left(\frac{\nu_t}{\sigma_\Sigma} \frac{\partial \Sigma}{\partial x_i} \right) = S_\Sigma = S_g - S_a + S_{LAM} \quad (4.18)$$

where σ_Σ is the turbulent Schmidt number, ν_t is the turbulent kinematic viscosity, S_g is the production of the flame surface by turbulent rate of strain, and S_a is the annihilation of flame surface due to reactants consumption. The terms S_g and S_a can be computed as:

$$S_g = \alpha K_{eff} \Sigma \quad (4.19)$$

$$S_a = \beta \Sigma^2 \rho_{fu,fr} S_L / \rho_{fu} \quad (4.20)$$

In the formula above, K_{eff} represents the mean stretch rate of flame. The mean stretch rate of the flame K_{eff} is calculated via:

$$K_{eff} = K_t = \frac{\varepsilon}{k} C_k \quad (4.21)$$

K_t is a very crucial property since it largely affects the source term for the flame surface. Thus, it has a direct impact on the mean turbulent reaction rate. S_{LAM} stands for the contribution of laminar combustion to the generation of flame surface density. It

is calculated as sum of three term as follows:

$$S_{LAM} = S_{PROP} + S_{CURV} + S_{STR} \quad (4.22)$$

where S_{PROP} , S_{CURV} and S_{STR} in order represent the contribution of propogation, curvature and straining and they are expressed as follows:

$$S_{PROP} = -\nabla \cdot \left(\frac{\bar{\rho}}{\rho_{fr}} S_L \Sigma \vec{N} \right) \quad (4.23)$$

$$S_{CURV} = \frac{\bar{\rho}}{\rho_{fr}} S_L (\nabla \cdot \vec{N}) \Sigma \quad (4.24)$$

$$S_{STR} = (\nabla \cdot \vec{u} - \vec{N} \cdot \vec{N} : \nabla \vec{u}) \quad (4.25)$$

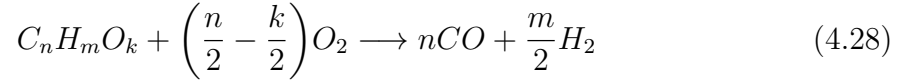
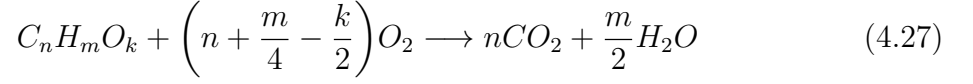
$$N = \frac{\nabla c}{|\nabla c|} \quad (4.26)$$

where c is reaction progress variable.

Stretching and quenching of flame surface density term S_Σ in equation 4.18 is on the basis of Intermittent Turbulence Net Frame Stretch (ITNFS) model [21] which describes vortex-flame front interactions by means of direct simulation.

4.1.3.1. Extended Coherent Flame Model(ECFM). This model can be thought as the extended version of the CFM previously described. Beside being fully coupled to spray model, it also provides stratified combustion modeling which involves EGR effects and NO formation. The basis of the model lies in a conditional unburned/burnt description of the thermochemical properties of the gas. This model can also be further extended with ECFM-3Z (3Z stands for 3 Zones) which includes general species treatment or separate CO/CO₂ oxidation reaction mechanism. Thus, it is possible to implement all

standard engine applications at once with only one combustion model. The model uses 2-step chemical reaction mechanism in fuel conversion as follows:



The reaction rate of the first reaction is calculated via:

$$\omega_{fu,1} = \omega_L \gamma \quad (4.29)$$

With the γ multiplier which is a function of the equivalence ratio ϕ and number of carbon and hydrogen atoms. For the second fuel conversion reaction, the rate is given as:

$$\omega_{fu,2} = \omega_L (1.0 - \gamma) \quad (4.30)$$

where ω_L represents the mean laminar fuel consumption rate expressed as follows:

$$w_L = \rho_{fu,fr} S_L \quad (4.31)$$

To calculate the reaction rates of each individual participants i for the reaction mechanism, the following is used:

$$\omega_i = \sum_{r=1}^2 \nu_{i,r} \omega_{fu,r} \quad (4.32)$$

where $\nu_{i,r}$ stands for the stoichiometric coefficients of species i in the reaction r .

With the same concept as in CFM, the mean turbulent fuel consumption rate is calculated as the multiplication of the flame surface density Σ and the laminar burning

velocity S_L as:

$$\overline{\rho \dot{r}_{fu}} = -\Sigma \sum_{r=1}^2 \nu_{i,r} \omega_{fu,r} = -\omega_L \gamma \Sigma \quad (4.33)$$

$$\overline{\rho \dot{r}_{fu}} = -\Sigma \sum_{r=1}^2 \nu_{i,r} \omega_{fu,r} = -\omega_L (1.0 - \gamma) \Sigma \quad (4.34)$$

Note that equation 4.33 and 4.34 are, in order, used for reaction-1 and for reaction-2.

Transport equations for ECFM are described by taking the concentration in the unburned and burnt gases separately into account. Furthermore, a source term S_{evap} is added for spray applications, thus there are two transport equations, one for fuel and another for oxygen, for the model as follows:

$$\frac{\partial}{\partial t}(\rho y_{fu,fr}) + \frac{\partial}{\partial x_j}(\rho u_j y_{fu,fr}) - \frac{\partial}{\partial x_j} \left(\frac{\mu_{eff}}{\sigma_i} \frac{\partial y_{fu,fr}}{\partial x_j} \right) = S_{evap} \quad (4.35)$$

$$\frac{\partial}{\partial t}(\rho y_{Ox,fr}) + \frac{\partial}{\partial x_j}(\rho u_j y_{Ox,fr}) - \frac{\partial}{\partial x_j} \left(\frac{\mu_{eff}}{\sigma_i} \frac{\partial y_{Ox,fr}}{\partial x_j} \right) = 0 \quad (4.36)$$

The following transport equation is further introduced for the unburned gas enthalpy as:

$$\frac{\partial}{\partial t}(\rho h_{fr}) + \frac{\partial}{\partial x_j}(\rho u_j h_{fr}) - \frac{\partial}{\partial x_j} \left(\frac{\mu_{eff}}{\sigma_i} \frac{\partial h_{fr}}{\partial x_j} \right) = \rho \varepsilon + \frac{\rho}{\rho_{fr}} \frac{\partial p}{\partial t} + h_{evap} \quad (4.37)$$

where h_{evap} is the source term for evaporation and σ represents the surface tension.

The unburned gas phase is the composition of 5 species which are fuel, oxygen, molecular nitrogen, carbon dioxide and water, while 11 species- O, O₂, N, N₂, H, H₂, CO, CO₂, water, OH and NO-form the burnt gas phase. In this model, equation 4.1, the species transport equation, have been applied to all these individual species.

Gas fractions $y_{fu,fr}$ and $y_{O_2,fr}$ are used to compute the richness of the fresh gas like:

$$\phi_{fr} = \alpha_{fu} \frac{y_{fu,fr}}{y_{O_2,fr}} \quad (4.38)$$

With α representing the constant stoichiometric function of the considered fuel.

4.1.3.2. Extended Coherent Flame Model 3-Zones(ECFM-3Z). This model has been developed especially for diesel combustion. 3Z stands for three zones namely unmixed air, unmixed fuel and mixed air-fuel zones in burned and unburned gas cells as shown below. The model is based on a flame surface density transport equation and a mixing model which is capable of describing inhomogeneous turbulent premixed and diffusion combustion. Compared to the ECFM previously described, this model has been further extended to cover an improved burnt gas chemistry description.

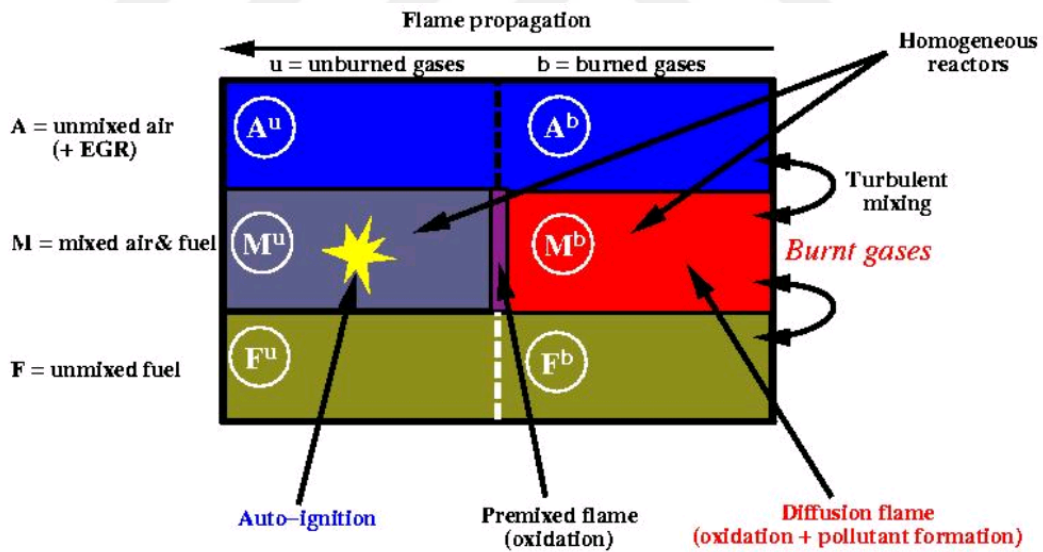


Figure 4.3. Zones in ECFM 3Z.

$$\frac{\partial \bar{\rho} \tilde{y}_k}{\partial t} + \frac{\partial \bar{\rho} \tilde{u}_i \tilde{y}_k}{\partial x_i} - \frac{\partial}{\partial x_i} \left(\left(\frac{\mu}{Sc} + \frac{\mu_t}{Sc_t} \right) \frac{\partial \tilde{y}_k}{\partial x_i} \right) = \bar{\omega}_k \quad (4.39)$$

Note that the superscript "–" represents ensemble-averaged quantity as "∼" stands for density weighted ensemble-averaged quantity.

Three new tracers, for NO, CO and H₂, are considered in the ECFM-3Z together with two species which describes the mixing fuel and oxygen. Furthermore, an intermediate species for auto-ignition is taken into account. The transport equations in this model is solved for the average quantities of O₂, N₂, CO₂, CO, H₂, H₂O, O, H, N, OH and NO in accordance with the equation 4.39. In the equation 4.39, $\bar{\omega}_k$ is the combustion source term and \bar{y}_k is the averaged mass fraction of species k .

The calculation of the ignition delay time, τ_d , is done in accordance with the following equation.

$$\tau_d = 4.804 \cdot 10^{-8} \left(N_{O_x}^{u,M} |_{u,M} \right)^{-0.53} \left(N_{F_u}^{u,M} |_{u,M} \right)^{-0.05} (\bar{\rho}^u)^{0.13} e^{\frac{5914}{T^u}} \quad (4.40)$$

where $N_{O_x}^{u,M} |_{u,M}$ is the molar concentration of oxidizer(oxygen) in unburned, mixed zone as $N_{F_u}^{u,M} |_{u,M}$ is the molar concentration of fuel in unburned, mixed zone.

The oxidation kinetics of the fuel is divided into two phases. For the first phase of the oxidation, it is considered that a first partial oxidation of fuel is considered which leads to the formation of a considerable amount of CO and some CO₂ in the burned gases of the mixed zone. In the second phase, CO previously formed is oxidized to CO₂. This oxidation approach provides more accurate results for the formation of CO in lean mixtures. Considering the used fuel, $C_n H_m O_k$, the following correlations give the local mean equivalence ratio $\bar{\phi}$:

$$\alpha = 1, \text{ if } \bar{\phi} < \bar{\phi}_1 = 0.99 \quad (4.41)$$

$$\alpha = \frac{3.92 \left(n + \frac{m}{4} - \frac{k}{2} \right)}{2n + m} - 2n, \text{ if } \bar{\phi}_1 < \bar{\phi} < \bar{\phi}_2 = 0.9\phi_{crit} \quad (4.42)$$

$$\alpha = 0, \text{ if } \bar{\phi}_2 < \bar{\phi} \quad (4.43)$$

where α is the CFM constant and the critical equivalence ratio ϕ_{crit} is defined as the equivalence ratio above which there is not enough oxygen to complete the oxidation of fuel into CO and it is calculated via:

$$\phi_{crit} = \frac{2}{n} \left(n + \frac{m}{4} - \frac{k}{2} \right) \quad (4.44)$$

4.2. Emission Models

4.2.1. Extenden Zeldovich Mechanism for NO_x Modeling

In diesel engines, nitric oxide emissions are significant due to the elevated temperatures reached within the cylinder. The formation of these molecules stem from three major reasons. The first kind of NO formation called "Thermal NO" is arised from the disassociaciation of the moleculariar-nitrogen. Second form is named "Prompt NO" and it is formed by the hydrocarbon fragments- air nitrogen interactions. The third form of nitric oxide is composed by the nitrogen content in the fuel. Fuel-NO and prompt NO formation can be neglected since they take up the minority of the total NO formation for diesel fuel combustion. Thus, in NO formation modeling, only thermal NO formation is considered. A very high temperatures or energy is needed to decompose the bonds of molecular N₂. In diesel engines, temperatures rise above 1800 K which is enough to surpass the activation energy for the initiation of thermal NO formation reactions.

In order to obtain pollutant formation precisely, one has to put the local temperature, pressure and the gas composition of the complex chemical schemes into consideration. In ECFM, these complex chemical reaction steps and species are kept limited for saving computation time and it is assumed that there is no fuel in the burnt gas phase.

Table 4.1. NOx model reaction rate constants.

k_{1f}	$1.8 \cdot 10^8 e^{-38.370/T}$
k_{1b}	$3.8 \cdot 10^7 e^{-425/T}$
k_{2f}	$1.8 \cdot 10^4 T e^{4680/T}$
k_{2b}	$3.8 \cdot 10^3 T e^{-20.82/T}$
k_{3f}	$7.1 \cdot 10^7 e^{-450/T}$
k_{3b}	$1.7 \cdot 10^8 e^{-24.56/T}$

The following reaction mechanism computes the NO formation and it is also known as extended Zeldovich mechanism [22]:



It can be seen that only five chemical species- O, H, OH, N and O₂- are considered for the thermal NO formation. First four chemical reactions above were proposed by Zeldovich and later the remaining ones were added to take the formation in fuel rich regions. Apparently, all reactions above highly depend on temperature, residence time and atomic oxygen concentration. Within the context of Extended Zeldovich Mechanism, the following equation gives the concentration of the formed thermal NO:

$$\frac{\partial N_{NO}}{\partial t} = k_{1f} N_O N_{N_2} + k_{2f} N_N N_{O_2} + k_{3f} N_N N_{OH} - k_{1b} N_{NO} c_N - k_{2b} N_{NO} N_O - k_{3b} N_{NO} N_H \quad (4.51)$$

where c represents concentration in mol/cm^3 . Table 4.1 shows the reaction rate constants for the model.

4.2.2. Soot Formation and The Hiroyasu/Nagle/Strickland-Constable Model

Carbonaceous particles-soot- are formed under high temperature and fuel rich conditions, which is conventionally found in diesel engine combustion process. The process of soot particle formation is composed of a number of chemical and physical stages such as formation and growth of large aromatic hydrocarbons, then their transformation into particles. Theoretically, soot is most likely formed when the equivalence ratio is greater than 1 or the air excess ratio is less than 1. In the literature, four major processes are described for soot formation which are called nucleation, coagulation, surface growth and oxidation. The local air-fuel ratio, C/H ratio, C/O ratio, temperature, pressure and residence time play a key role for soot formation. It is a fact that amount of soot increases up to 1600 K and then its concentration decreases due to the increased oxidation.

In the present study, soot has been modeled according to soot oxidation concept proposed by Hiroyasi et. al. [23]. Rate of soot formation is calculated as:

$$\frac{dm_s}{dt} = \frac{dm_{sf}}{dt} - \frac{dm_{so}}{dt} \quad (4.52)$$

$$\frac{dm_{sf}}{dt} = A_f m_{fg} p^{0.5} \exp\left(\frac{-E_{sf}}{RT}\right) \quad (4.53)$$

$$\frac{dm_{so}}{dt} = A_o m_s p^{1.8} \exp\left(\frac{-E_{so}}{RT}\right) \quad (4.54)$$

where E_{sf} and E_{so} are, in order, the activation energy for soot formation and soot oxidation. Note that m_{fg} is mass of gaseous fuel, m_s is mass of soot particles, A_f and A_o are soot formation and soot oxidation constants, respectively.

Figure 4.4 shows NO and soot emission regions with respect to the equivalence ratio. It can be said that for soot formation, the temperature in the combustion zone

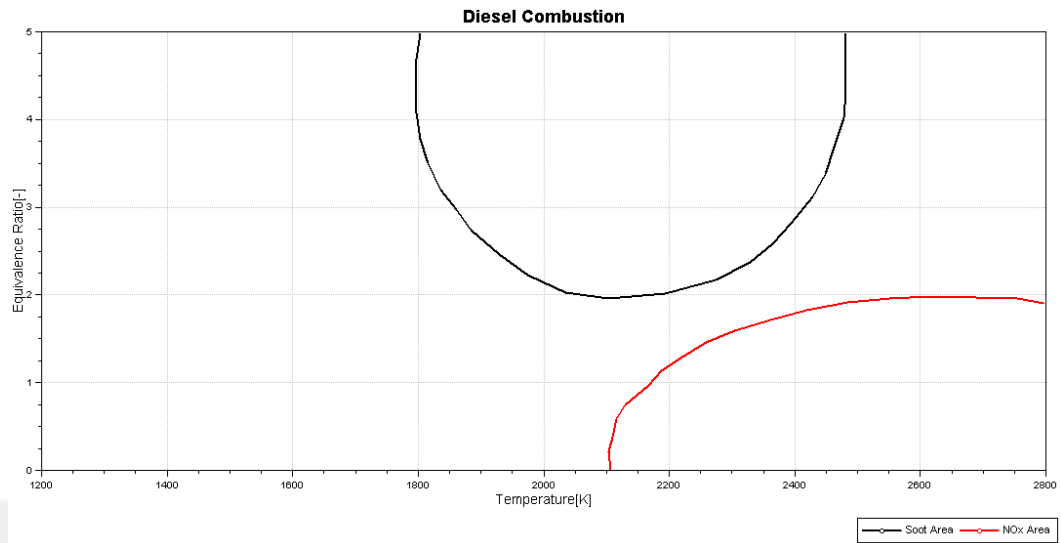


Figure 4.4. Regions for NO and soot emissions (Equivalence ratio) [6].

should be between 1800 K and 2500 K and the equivalence ratio should be higher than 2. As for NO formation, the temperature should be over 2100 K and the equivalence ratio should be lower than 2.

4.3. Spray Models

Spray simulation requires the numerical solution of conservation equations for the gas and the liquid state together with the multi-phase flow concept. Spray calculations in engineering are based on Discrete Droplet Method (DDM) which is a statistical method [24]. In this method, ODEs are solved for the trajectory, momentum, heat and mass transfer of single droplets regarded as a member of a “parcel” formed by identical non-interacting droplets. These parcels are specified in the flow domain by defining the initial conditions of position, size, velocity, temperature and number of particles in the parcel. Then, spray atomization processes – which include droplet-gas momentum exchange, turbulent dispersion, evaporation of droplets, secondary-break-up, droplet collision and droplet-wall interactions are solved by means of a number of submodels. Figure 4.5 shows the stages of a spray breakup regime in a cylinder.

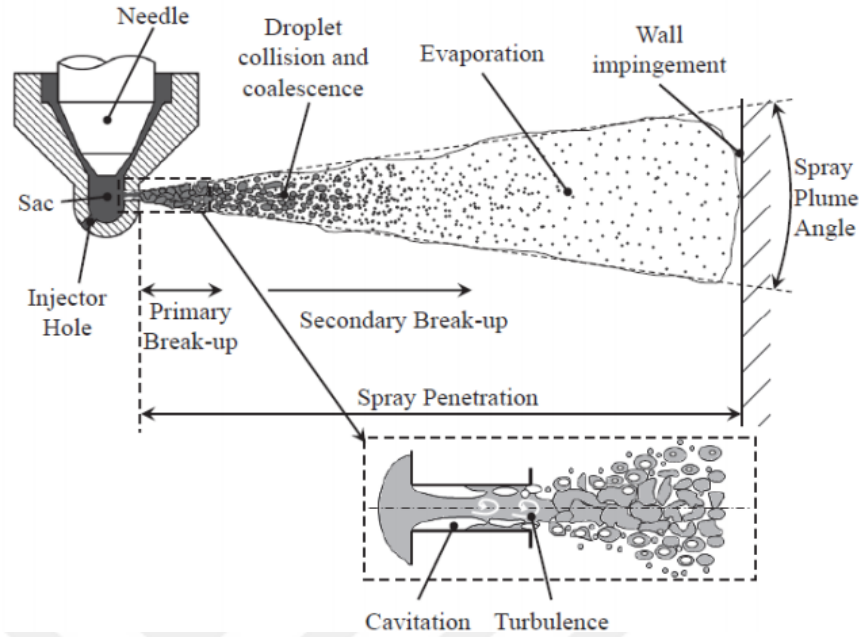


Figure 4.5. Stages of high-pressure diesel spray breakup [7].

Considering that the combustion phase is governed by the spray propagation, injection timing and injection rate map play a key role in diesel engine combustion process. Fuel injection conventionally starts about 20 CA before the TDC and it ends after the TDC [3]. Injection rate map denotes the rate of change of injected fuel during the injection period. There are different kind of profiles. The optimum injection rate maps have been shown in the Figure 4.6. It has been proposed that in low-load region, a square-shaped rate is used. As for the high load region, a boot shape profile is chosen while the ramp-shaped profile is preferred for the medium-load conditions. It is also asserted that injection rate map should be a squared-shape at high engine speed regardless of the engine load [5].

4.3.1. Mathematical Equations

The trajectory and velocity of a particle/droplet/parcel is calculated by following momentum equation:

$$m_d \frac{du_{id}}{dt} = F_{idr} + F_{ig} + F_{ip} + F_{ivm} + F_{ib} \quad (4.55)$$

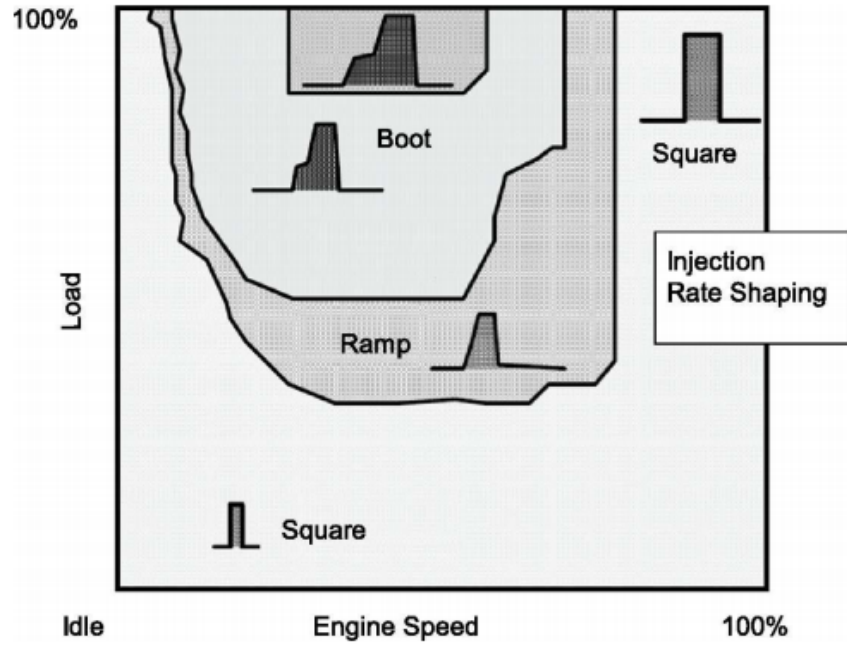


Figure 4.6. Injection-rate shape map [5].

where the drag force F_{idr} is computed by:

$$F_{idr} = \frac{1}{2} \rho_g A_d C_D |u_{rel}| u_{irel} \quad (4.56)$$

and other force components in the momentum equation are calculated by:

$$F_{ig} = V_p (\rho_p - \rho_g) g_i \quad (4.57)$$

$$F_{ip} = -V_p \nabla p \quad (4.58)$$

$$F_{ivm} = 0 \quad (4.59)$$

$$F_{ib} = 0 \quad (4.60)$$

Taking all these expressions into account together with virtual mass force components F_{ivm} and F_{ib} like magnetic or electrostatic forces and so forth, the momentum equation

takes its final form as:

$$\frac{du_{id}}{dt} = \frac{3}{4}C_D \frac{\rho_g}{\rho_d} \frac{1}{D_d} |u_g - u_d|(u_{ig} - u_{id}) + \left(1 - \frac{\rho_g}{\rho_d}\right)g_i \quad (4.61)$$

By integrating the equation above, the instantaneous velocity and the position of a particle can be found. Note that u_{rel} , u_g and u_d are, in order, the relative velocity of droplet, absolute velocity of gas and absolute velocity of droplet.

4.3.2. Evaporation Model

Derived by Dukowicz [25], this evaporation model assumes that droplets have spherical symmetry, temperature along the droplet diameter is uniform, physical properties of the surrounding fluid is uniform and also it assumes that there is a liquid-vapor thermal equilibrium and quasi steady gas-film around droplet surface. Due to the assumption of uniform droplet temperature, the change in temperature is determined by energy balance equation, which expresses that the energy flow through the droplet either heats it up or causes it to vaporize. In the model, it is also considered that the droplet is evaporating in a non-condensable gas. Thus, it uses two separate, non-mixing regions in gas-phase namely vapor and non-condensable gas domain. Energy equation for a droplet is as follows:

$$m_d c_{pd} \frac{dT_d}{dt} = L \frac{dm_d}{dt} + \dot{Q} \quad (4.62)$$

where convective heat flux \dot{Q} from the surrounding gas to the droplet surface is given by:

$$\dot{Q} = \alpha_{cnv} A_s (T_\infty - T_s) \quad (4.63)$$

With the assumption of droplet surface uniformity, the governing equation for mass flux can be written as follows after introducing the local surface heat flux, \dot{q}_s , and the

vapor mass flux, \dot{f}_{vs} :

$$\frac{dm_d}{dt} = \dot{Q} \frac{\dot{f}_{vs}}{\dot{q}_s} \quad (4.64)$$

Accordingly, the droplet energy equation can be written as:

$$m_d c_{pd} \frac{dT_d}{dt} = \dot{Q} \left(1 + L \frac{\dot{f}_{vs}}{\dot{q}_s} \right) \quad (4.65)$$

Introducing the ratio of $\frac{\nabla_s y_v}{\nabla_s T}$, the ratio of the vapor mass flux to the surface heat flux can be re-expressed as follows:

$$\frac{\dot{f}_{vs}}{\dot{q}_s} = \frac{\rho \beta}{k} \left(\frac{1}{1 - y_{v,s}} \right) \frac{\nabla_s y_v}{\nabla_s T} \quad (4.66)$$

In the equation above, L is the latent heat of evaporation, β is binary diffusion coefficient and k is reaction rate, $\nabla_s y_v$ is vapor mass fraction derivative in the direction normal to the droplet surface and $\nabla_s T$ is near droplet temperature derivative in the direction normal to the droplet surface. Note that the ratio $\frac{\nabla_s y_v}{\nabla_s T}$ is expressed as:

$$\frac{\nabla_s y_v}{\nabla_s T} = \frac{c_p}{Le \left(\frac{h_\infty - h_s}{y_{v,\infty} - y_{v,s}} - h_{v,s} - h_{g,s} \right)} \quad (4.67)$$

Assuming that the Lewis number is unity ($Le = 1$), the flux ratio can be expressed with its final form as follows [25]:

$$\frac{\dot{f}_{vs}}{\dot{q}_s} = \frac{-B_y}{h_\infty - h_s - (h_{sv} - h_{gs})(y_{v\infty} - y_{vs})} \quad (4.68)$$

where B_y is defined as:

$$B_y = \frac{y_{vs} - y_{v\infty}}{1 - y_{vs}} \quad (4.69)$$

Note that h_∞ is the enthalpy at particle far-field, h_s is the enthalpy at droplet surface, h_{sv} is vapor enthalpy at droplet surface and h_{gs} is the enthalpy of gas at droplet surface.

4.3.3. Wave Break-up Model

Within this model, it is assumed that the development of an initial perturbation on a liquid surface is correlated to its wavelength and other physical and dynamic variables of the injected fuel and the fluid [26]. There are two break-up regimes, one of which is for high velocities and the other is for low velocity Rayleigh type break-up. For the first type, it is considered that the diameter of the product droplet equals to the wavelength of the fastest growing or most probable unstable surface wave. The second type break-up regime produces droplets with larger diameter than its parent drop. This type of regime has not significant importance for high pressure injection systems. In this model, the droplet radius reduction is calculated via:

$$\frac{dr}{dt} = -\frac{(r - r_{stable})}{\tau_a} \quad (4.70)$$

where τ_a is the break-up time defined as:

$$\tau_a = \frac{3.726.C_2.r}{\Lambda.\Omega} \quad (4.71)$$

The radius of the product droplet r_{stable} is proportional to the wavelength Λ of the fastest growing wave on the liquid surface. These terms and the wave growth rate Ω are defined as:

$$r_{stable} = C_1\Lambda \quad (4.72)$$

$$\Lambda = 9.02r \frac{(1 + 0.45.Oh^{0.5}).(1 + 0.4T^{0.7})}{(1 + 0.87.We_g^{1.67})^{0.6}} \quad (4.73)$$

$$\Omega = \left(\frac{\rho_d r^3}{\sigma} \right)^{-0.5} \frac{0.34 + 0.38.We_g^{1.5}}{(1 + Oh)(1 + 1.4T^{0.6})} \quad (4.74)$$

Note that We is Weber number and Oh is Ohnesorge number.

4.3.4. Turbulence Model

In the present study, the $k - \varepsilon$ turbulence model is used. The model has been chiefly utilized and implemented in most CFD codes and it has been tested in a variety of flows such as heat transfer, combustion and two-phase flows. The model, in which k is the turbulent kinetic energy and ε is the turbulent dissipation, predicts reasonably realistic results. The following equations are applied over a control volume:

$$\rho \frac{Dk}{Dt} = P + G - \varepsilon + \frac{\partial}{\partial x_j} \left(\mu + \frac{\mu_t}{\sigma k} \frac{\partial k}{\partial x_j} \right) \quad (4.75)$$

$$\rho \frac{D\varepsilon}{Dt} = \left(C_{e1}P + C_{e3}G + C_{e4}k \frac{\partial U_k}{\partial x_k} - C_{e2}\varepsilon \right) \frac{\varepsilon}{k} \frac{\partial}{\partial x_j} \left(\frac{\mu_t}{\sigma_e} \frac{\partial \varepsilon}{\partial x_j} \right) \quad (4.76)$$

$$P = 2\mu_t S.S - (2/3)[\mu_t(trS) + k](trS) \quad (4.77)$$

$$\mu_t = C_\mu \rho \frac{k^2}{\varepsilon}; \quad G = -\frac{\mu_t}{\rho \sigma_p} \nabla \rho \quad (4.78)$$

The coefficients used in the turbulence model are tabulated above.

Table 4.2. Turbulence model constants.

	C_μ	C_{e1}	C_{e2}	C_{e3}	C_{e4}	σ_k	σ_e	σ_ρ
Values	0.09	1.44	1.92	0.8	-3.373	1	1.3	0.9

5. SIMULATION AND RESULTS

In this study, multidimensional combustion modeling has been done by using AVL FIRE software. The name of the CI diesel engine studied is PumaGlobal(2.2 liters 125hp) produced by Ford Motor Company.

5.1. Geometrical Description

Geometrically embodiment of the domain to be studied is the first step to whole simulation process. Within this context, general engine parameters such as the type of engine, number of cylinder, piston moving specification have been set as shown in the Table 5.1. After all required parameters are specified, in cylinder geometry which is confined within the borders of piston bowl, piston head, cylinder head, cylinder wall and injector is to be defined. To do so, AutoCAD software has been used to draw the geometry then the sketch has been imported into AVL FIRE program.

Table 5.1. General engine configurations.

Engine Name	PumaGlobal
Engine layout	Inline
Number of cylinders [-]	4
Bore [m]	0.08600
Compression Ratio [-]	15.50000
Crank radius [m]	0.04730
Connecting rod length [m]	0.15500
Stroke [m]	0.09460

Table 5.2. General injector parameters.

Number of nozzles [-]	8
Injector distance l_w [m]	0.00080
Injector tip protrusion l_h [m]	0.00160
Inj. nozzle position Z-coordinate [m]	0.00050
Nozzle hole outer diameter [m]	0.00016
Nozzle hole outer diameter [m]	N/A
Nozzle hole half outer cone angle [deg]	7.50000
Inj. spray delta angle [deg]	140

5.1.1. Injector Geometry

Geometrical description of injector is important for both the definition of the computational domain and the spray modeling which directly affects the overall combustion process. Injection features such as the position of the injection and its orientation (spray angle, direction etc.) are shown in the Table 5.2 , general injector specifications have been shown.

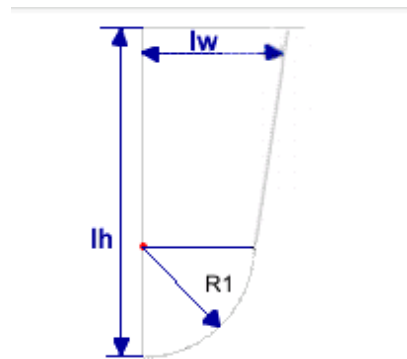


Figure 5.1. Injector template.

5.1.2. Final Geometry

When all geometrical components and definitions come together, the final computational domain for the simulation has been completed as shown in Figure 5.2. Note

that the crevice space is 6mm and the actual compression ratio for the cylinder is 17.56 after the definition of the injector and the piston bowl. Note that the red dashed-line indicates the spray injection projection.

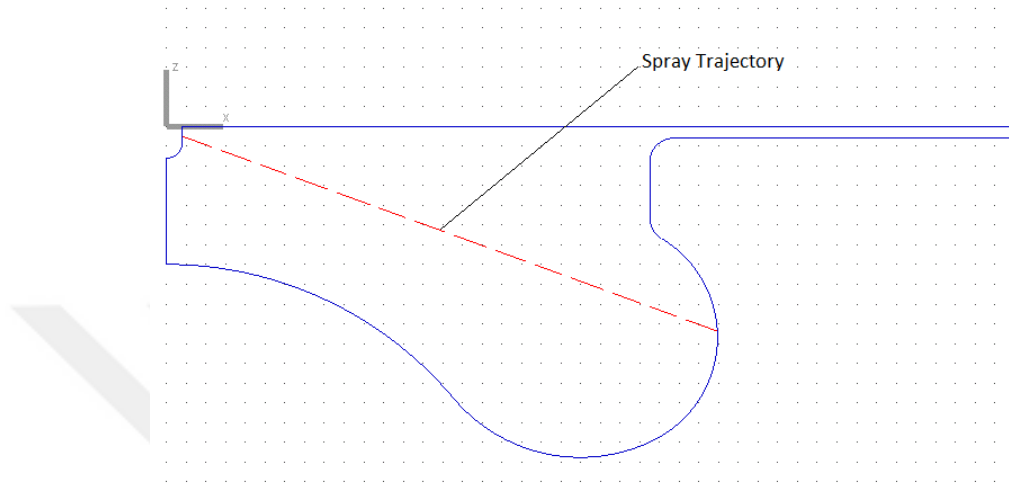


Figure 5.2. In cylinder computational domain.

5.2. Domain Discretization

Discretization has been done to the domain. Hexahedral mesh type has been preferred since they best fit and meet the simulation purpose. There are mainly four different blocks, which are namely, injector block, spray block, cylinder block and piston bowl block as it is shown in the Figure 5.3. Note that during the simulation, only cylinder block is expanding and contracting. Whole piston bowl domain considered as a single unit then divided into small parcels, so-called meshes, then two boundary layers have been defined, one of which is for the piston and the other is for the cylinder. Boundary layer thicknesses have been set to 0.00005 m. Taking the experimental data, PFP and mean effective pressures into account, average cell size has accordingly been determined as 0.0006 m to obtain a good agreement between simulation and experimental result. After mesh quality check process in which the aspect ratios and the skewnesses are checked, the generated mesh quality is verified to be appropriate to get convergent simulation results. Table 5.3 shows mesh data.

Table 5.3. Mesh data.

Mesh type	Hexahedron
Total number of meshes	202425
Average mesh size	6 mm
Max. skewness	1
Negative area	0

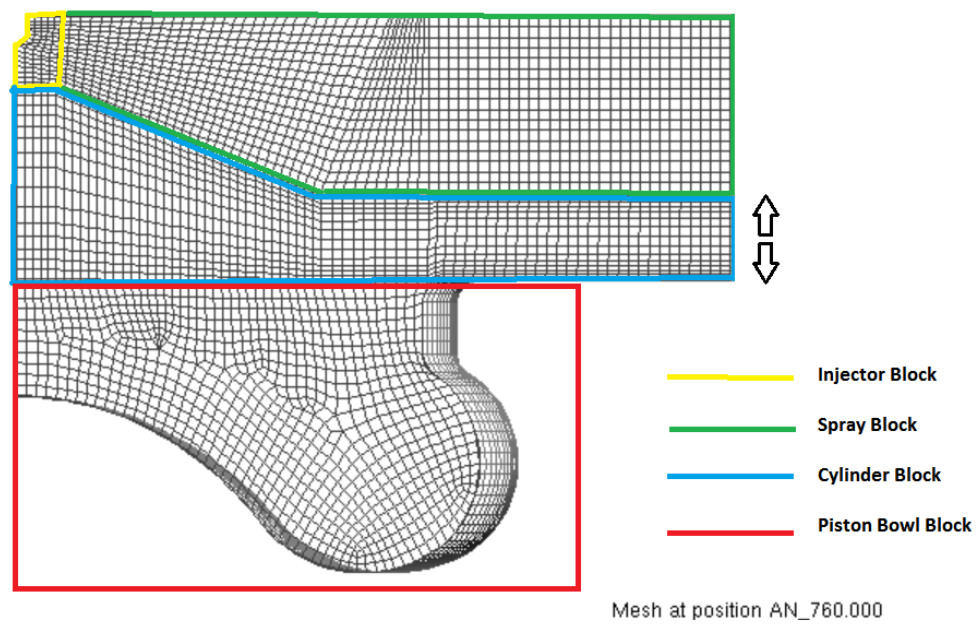


Figure 5.3. Mesh blocks in the computational domain.

5.3. Simulation Parameters

5.3.1. Run Mode

Simulation process proceeds which respect to crank angle. The simulation interval is set between 540 CA and 900 CA where piston is at BDC before the compression stroke and then again at the BDC after power stroke respectively. Time interval is set to 0.5 CA which means there are 720 different CA positions to be simulated during the entire combustion process. Within the run process, mainly, species transport, spray, combustion and emission will be solved.

5.3.2. Base-Line Simulation

First part of the engine simulations have been made for the validation. Within this context, the experimental data retrieved from Ford Motor Company for the PumaGlobal 2.2liters 125hp diesel engine-have been used. In the present study, engine speed has been selected as 3600 rpm at which the maximum power is achieved. In the Figure 5.4 engine power output which respect to the engine speed is shown.

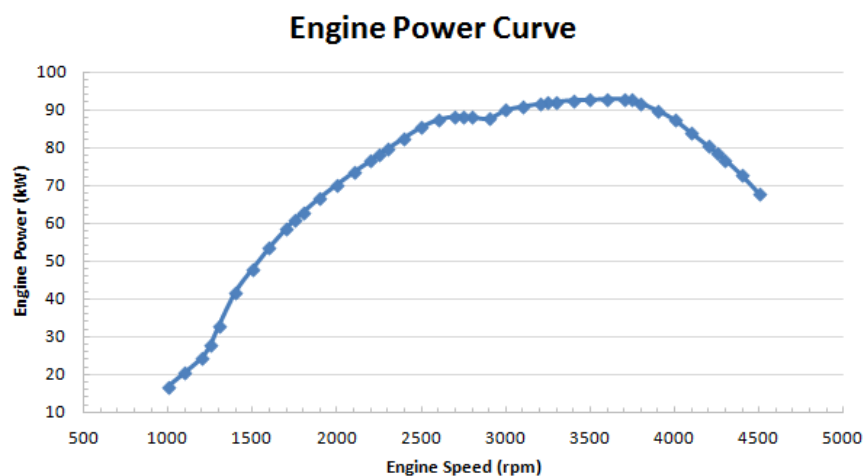


Figure 5.4. Engine power curve.

Table 5.4. Boundary conditions at 3600rpm.

Piston Head Temperature [K]	398.15
Liner Temperature [K]	410.15
Cylinder Head Temperature [K]	398.15

Table 5.5. Initial conditions at 3600rpm.

In-cylinder Air Pressure [Pa]	202561
In-cylinder Air Temperature [K]	433.7
In-cylinder Swirl Ratio [-]	1

5.3.2.1. Boundary Conditions. At domain boundaries, which is confined by the borders of piston and cylinder, temperature assumptions have been made and it has been also assumed that those temperatures remains constant during the cycle. At 3600 rpm engine speed, the Table 5.4 shows the boundary conditions. Note that the domain is cymetrical about the cylinder axis.

5.3.2.2. Initial Conditions. In the initial position of the system where piston is at the BDC, there is only inducted air to be compressed in the cylinder. In the base-line simulation the air swirl ratio is assumed to be 1 which means in-cylinder air is rotating about the cylinder axis at the speed of engine (3600rpm). Since the engine is turbocharged, the air inside the cylinder has been pressurized above the atmospheric pressure (100kPa). Table 5.5 summarizes the initial conditions. Note that the simulation will be performed with no EGR since the tested engine has no EGR system.

5.3.2.3. Simulation Models. During the simulation, the conservation equations (Mass, Momentum and Energy Equations) together with species transport equations are to be solved. As for the turbulence, the $k-\varepsilon$ model will be used. Air in the cylinder has been assumed to be compressible and ideal gas. Heat wall transfer will be calculated via the convective heat transfer equations. Note that there will be no radiation heat transfer calculations for the accumulated heat transfer through the cylinder walls. Maximum

and minimum number of iterations have been set, in order, to 50 and 5 for each crank-angle. Average error has been set to 0.001 for the pressure and momentum calculations. ECFM-3Z has been used for the combustion model due to its superior capabilities for diesel engine combustion. Diesel ($C_{13}H_{23}$) has been selected as fuel and, the extinction temperature is set to a very low level (200K) for the chemical reactions in order to eliminate frozen combustion reactions. Auto-ignition model has been used for the combustion initiation. The Extended Zeldovich emission model is to be used for NOx emissions, and it is the Hiroyasu Model for the soot modeling. Diesel spray has been modeled with Eulerian-Lagrangian Spray approach. Within this scope, Dukowicz evaporation, Wave Break-up and Walljet1 models have been used for the spray evaporation, spray break-up and spray-wall interactions respectively. These models have been covered in detail in Chapter 4. The injected fuel mass is 51.5 mg/stroke at 3600 rpm engine speed. Thus considering the number of holes on the injector (8), the injected fuel mass from each nozzle hole has been set to 6.438 mg/stroke. Injected liquid temperature is set to 330.15 K and injection timing is set to from 17 CA bTDC to 13 CA aTDC. Note that there is only main injection at 3600 rpm engine speed case and injection rate has been assumed to be uniform.

5.3.3. Validation of Base-line Simulation

The baseline simulation at 3600 rpm engine speed has been performed successfully. The boundary conditions like cylinder, piston wall temperatures, and initial conditions like in-cylinder air pressure and temperature data have been retrieved from a study conducted by Asma at Bogazici University [27]. The simulation results, in general, show a good agreement with the experimental data. Table 5.6 shows the comparison between the simulated and the experimental general engine data. Excellent match has been achieved for the peak firing pressure and the BMEP parameters. Relatively larger errors have been observed for the power and the torque output since the simulation does not cover the external factors such as engine powertrain and experimental test-bench components which affects those parameters.

Table 5.6. General engine output for 3600 rpm (Baseline).

Parameter	Simulation Results	Experimental Result	Error in %
AFR [-]	18.32	18.32	-
Peak Firing Pressure [Bar]	140.62	142.22	-0.11
BMEP [Bar]	14.76	14.09	+4.75
Power Output [kW]	101.4	92.88	+9.17
Torque Output [Nm]	268.8	307.6	-12.6

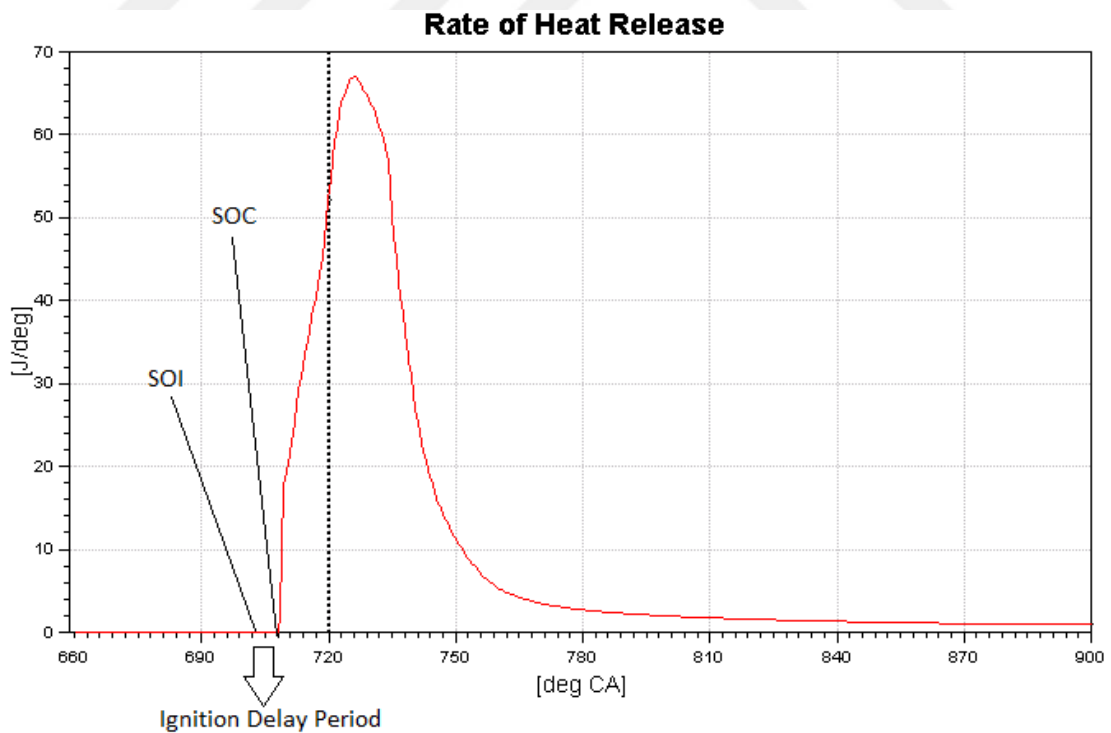


Figure 5.5. Baseline heat release rate curve at 3600rpm.

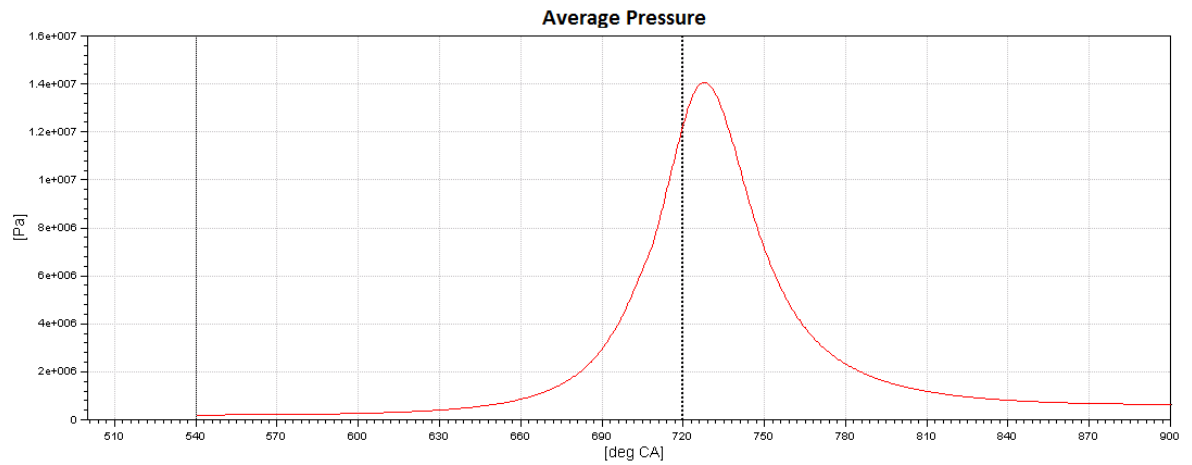


Figure 5.6. Baseline pressure curve at 3600rpm.

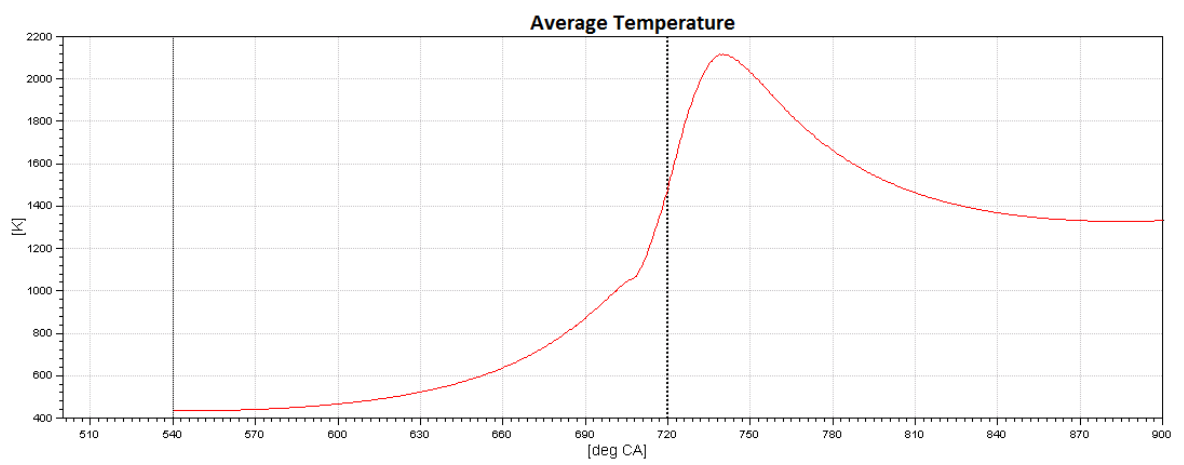


Figure 5.7. Baseline temperature curve at 3600rpm.

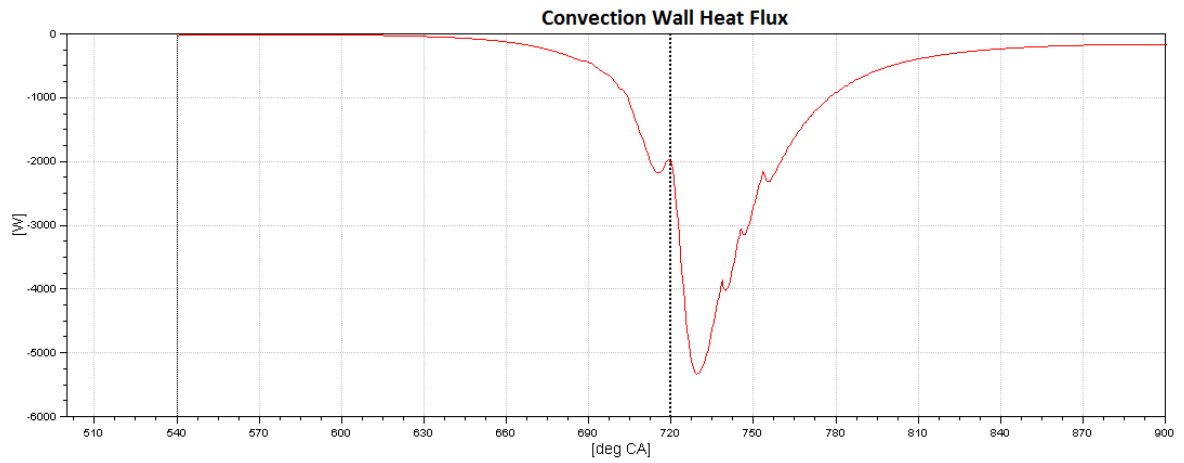


Figure 5.8. Baseline heatflux curve at 3600rpm.

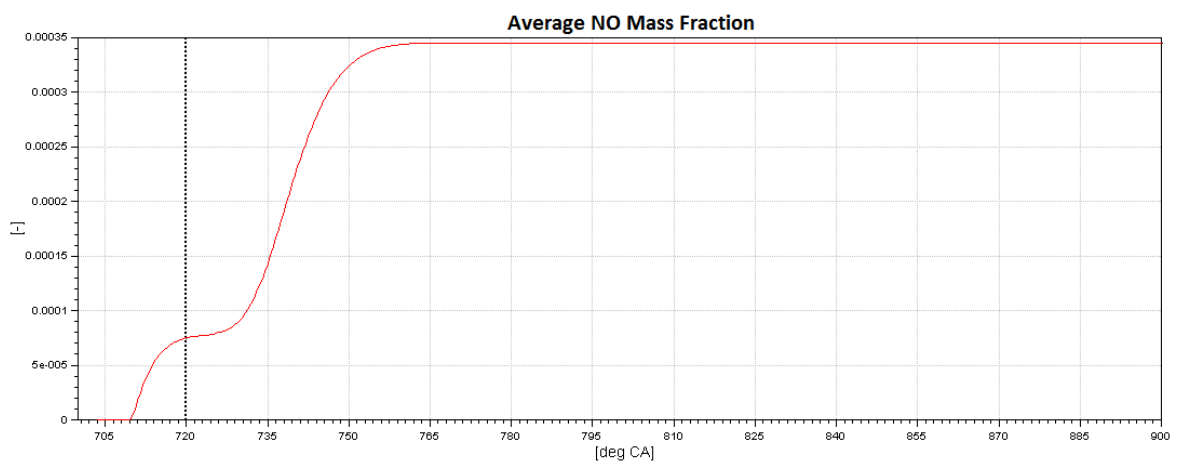


Figure 5.9. Baseline NO curve at 3600rpm.

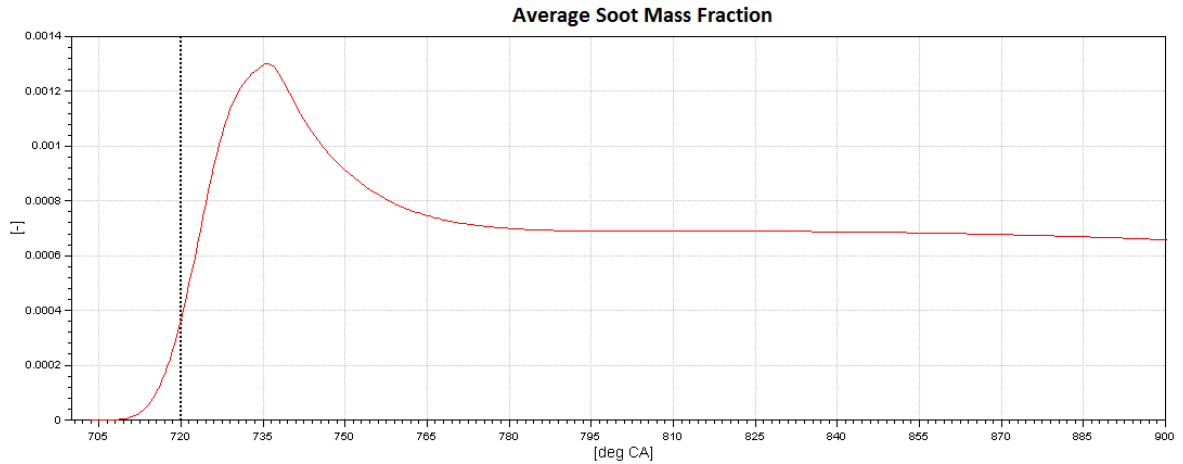


Figure 5.10. Baseline soot curve at 3600rpm.

5.3.3.1. Quantity Plots for Base-line Simulation at 3600 rpm. In the baseline simulation which injection starts at 17 CA bTDC and ends at 13 CA aTDC, the following output plots shows some detail about the combustion process. Figure 5.5 indicates that the rate of heat release has been firstly observed at 12 CA bTDC which means in this particular case, the ignition delay period takes about 5 CA or 0.23 milliseconds. After the rate of heat release shows an increase which means the initiation of the combustion process, the rate of increase of in-cylinder temperature rises up. In the Figure 5.6 and Figure 5.7, it can be observed that in-cylinder temperature and pressure rises to 2117 K and 141 bars respectively. It can be seen that wall heat flux, which is due to the convection heat transfer from in-cylinder fluids to the cylinder side wall, shows a rapid increase right after TDC (at 720 CA) where heat release rates and in-cylinder temperatures have dramatically elevated. Figure 5.9 shows that NO mass fraction rises due to the increasing in-cylinder temperature and it does not show a considerable change after 765 CA since the decomposition reaction rate is small. Figure 5.10 indicates that soot mass fraction rises up to about 735 CA then it starts decreasing since the remaining oxygen in the cylinder further oxidizes the soot particles.

5.3.3.2. 2D Countours at 3600 rpm. Figure 5.11 and 5.12 shows the local in-cylinder pressure and temperature distribution at 732 CA for the base-line case. It can be seen that the local dynamic pressures does not show a dramatic change from location to

location with respect to the total absolute pressure about 140bars. The maximum local pressure difference is read as 56.472 kPa which is too small compared to the absolute 1.4 MPa. The dynamic pressure variation in the cylinder contributes to the in-cylinder flows. It can be asserted that the total pressures slightly fluctuate about the absolute mean cylinder pressure value. However, local temperatures shows dramatic difference from region to region. In Figure 5.12, it can be seen that temperature reaches its a maximum value, 2426.4 K, and a minimum value of 804.28 K. Considering the average temperature at 732 CA, 2116K, it can be said that the local temperatures largely change with reference to the in-cylinder average temperature value.

From Fig. 5.13 to Fig. 5.16, 2D quantity contours have been shown for 720 CA, 732 CA, 738 CA and 750 CA, respectively. In each crank-angle case, local equivalence ratio, local temperature, local NO mass fraction and local soot mass fraction have been shown respectively. Figure 5.13 shows these quantities at 720 CA (TDC). The maximum equivalence ratio has been read as 4.13 and it is located in the center of spray where the maximum soot mass fractions have been observed. Temperatures rise up to 2340 K and the maximum NO emissions are seen near to the injector-cylinder head region since the temperatures and the equivalence ratios are proper for NO formation. In Figure 5.14, it can be seen that the spray has propagated through the injection trajectory. At this moment, the maximum equivalence ratio in the spray center has reduced to 3.70, which means the liquid fuel has evaporated and mixed with in-cylinder air. Soot density has been observed in the spray center. The temperatures have risen up to 2426 K and NO emissions location has slightly shifted towards the cylinder wall. At 738 CA, Figure 5.15 have shown that the spray has hit the combustion chamber wall and it has spread around. Note that the injection has already completed at 733 CA which means that from 733 CA on, the fuel-air mixing process is controlled by piston and in-cylinder charge motion. The equivalence ratio has further diminished to 2.14, which is a sign of fuel-air mixture in the cylinder. Temperatures have shown an increase up to 2533 K and NO region has further shifted towards the cylinder wall and it is now located between cylinder head and the piston head region. In the later stages of combustion, at 750 CA, the maximum temperature has reduced to 2494 K. The maximum equivalence ratio is observed around the swirl chamber. Parallel to this, the

soot region is seen around the swirl chamber. As for the NO formation, it has further moved to the cylinder wall.

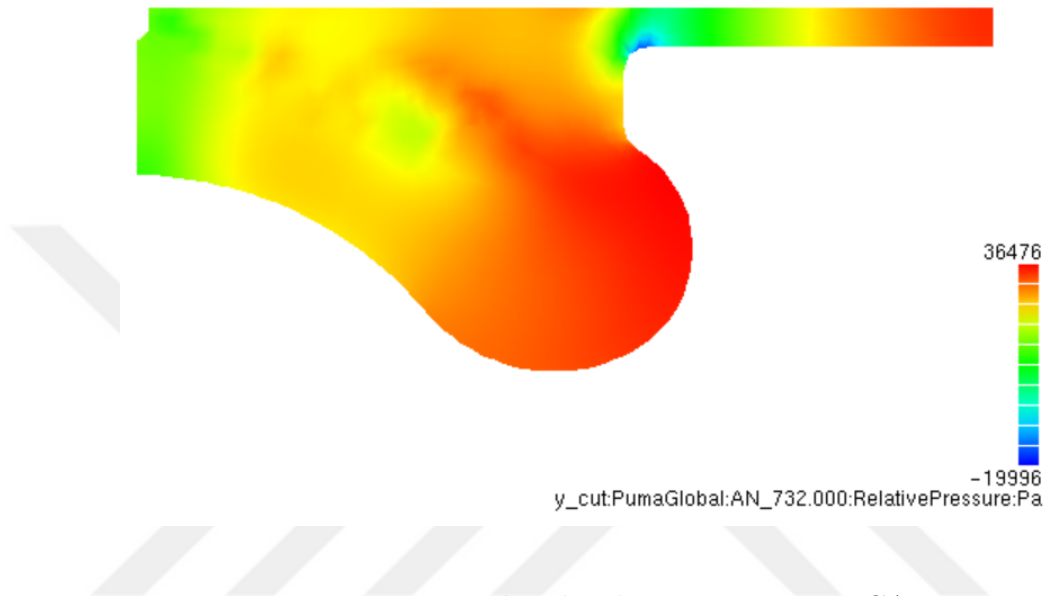


Figure 5.11. Baseline local pressures at 732 CA.

5.4. Investigation on the Effects of Various Swirl Ratio and Injection Timing on Combustion and Emissions

After the model validation, studies have continued to observe the effects of swirl ratio and injection timing on combustion and emission trends. Taking the base-line simulation as a reference, various swirl ratios and injection timings have been set accordingly. Table 5.7 summarizes the the parametric studies to be conducted. Note that the injection durations for each case are set to 30 CA (1.38 milliseconds).

5.4.1. Simulation Results for Swirl Ratio

As it has been discussed in the previous section, swirl is used to enhance the fuel-air mixing in the cylinder. Within this context, simulations have been performed for

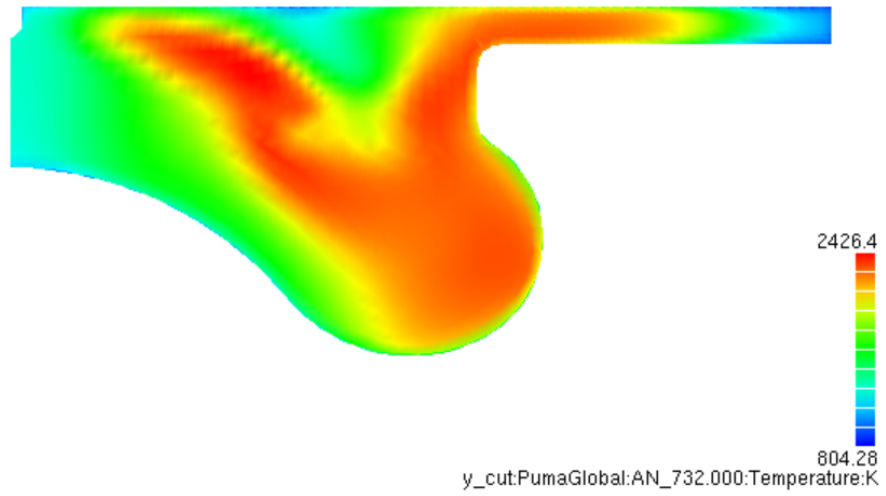


Figure 5.12. Baseline local temperatures at 732 CA.

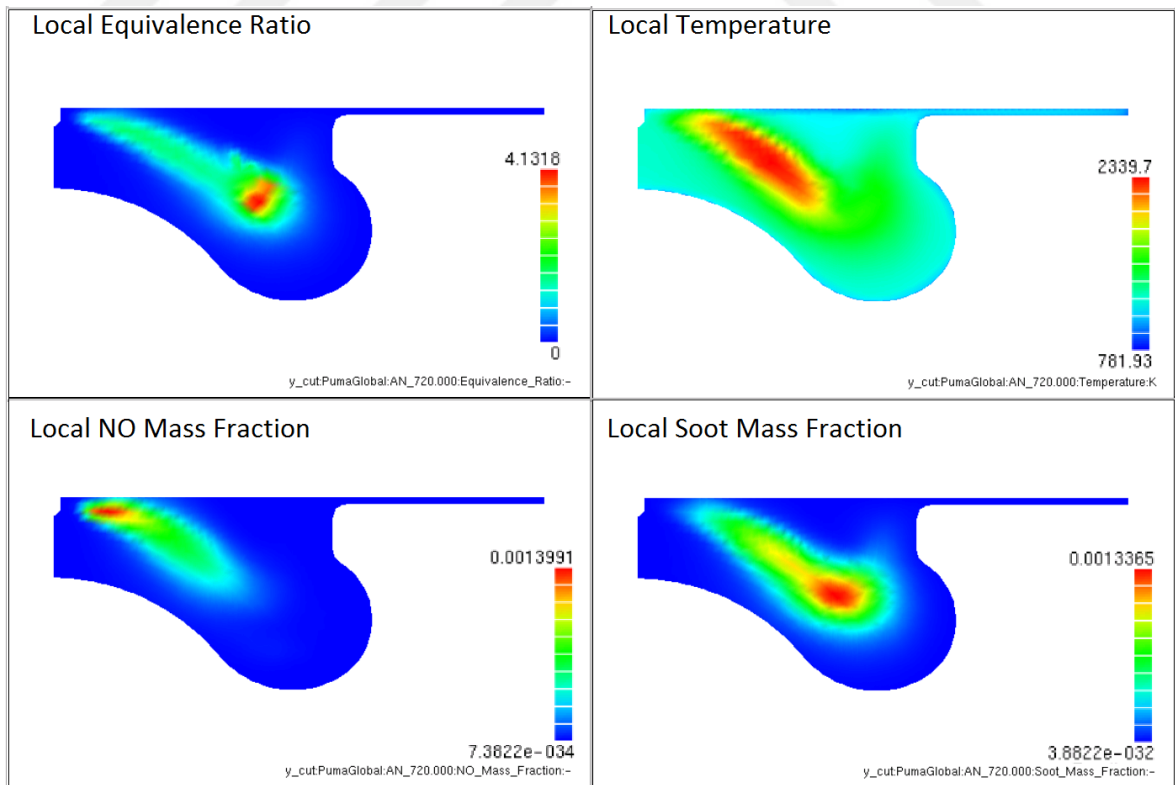


Figure 5.13. Quantity contours at 720 CA.

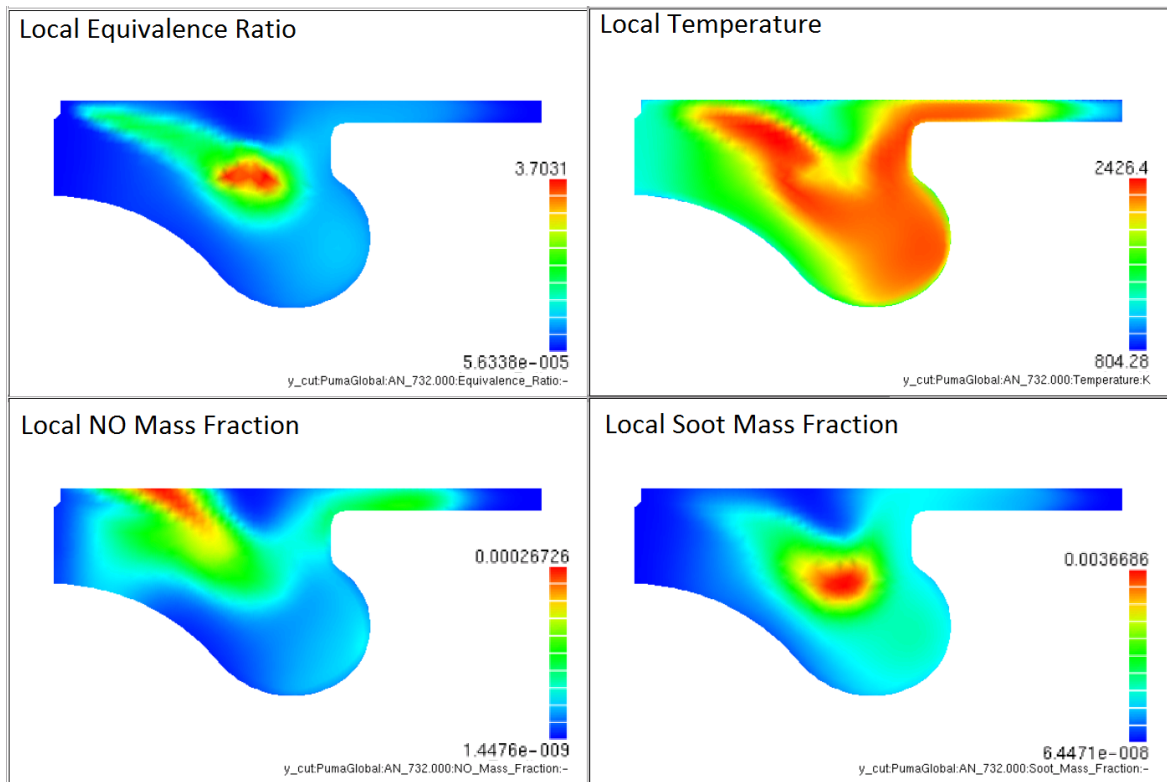


Figure 5.14. Quantity contours at 732 CA.

Table 5.7. Summary of the parametric study.

Case name	Swirl ratio	Start of Injection
Baseline	1.0	17 CA bTDC
SR 0.3	0.3	17 CA bTDC
SR 0.8	0.8	17 CA bTDC
SR 2	2.0	17 CA bTDC
SR 3	3.0	17 CA bTDC
Advanced injection	1.0	21 CA bTDC
Retarded injection	1.0	13 CA bTDC

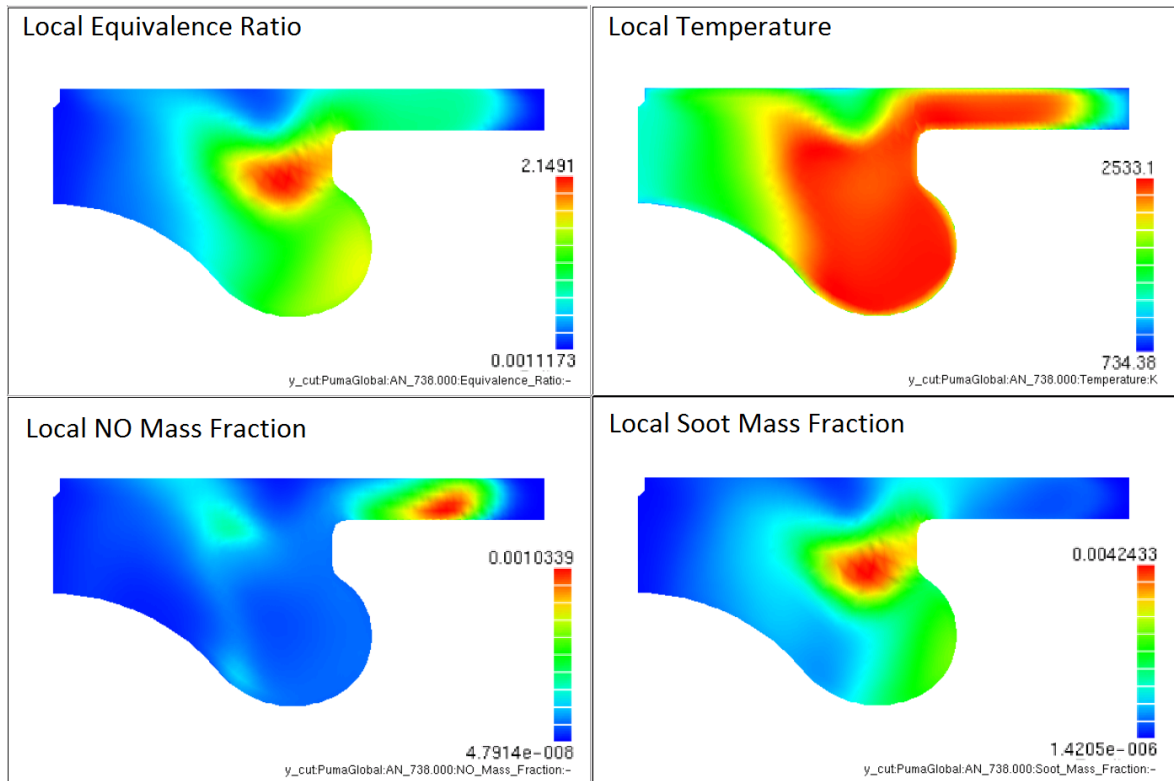


Figure 5.15. Quantity contours at 738 CA.

Table 5.8. General engine output comparison for swirl ratio.

Swirl Ratio [-]	0.3	0.8	1	2	3
A/F Ratio [-]	18.32	18.32	18.32	18.32	18.32
Injected Fuel Mass [mg]	51.5	51.5	51.5	51.5	51.5
BMEP [bar]	13.87	14.40	14.76	14.05	13.79
Bsfc [g/kW h]	243.4	234.4	228.6	240.1	244.8
Indicated Efficiency [%]	36	38	39	37	36
Indicated Power [kW]	23.86	24.73	25.34	24.17	23.73
NO mass fraction [$\times 10^{-4}$]	2.68	2.89	3.45	1.99	1.80
Soot mass fraction [$\times 10^{-3}$]	1.14	0.96	0.66	0.85	0.87

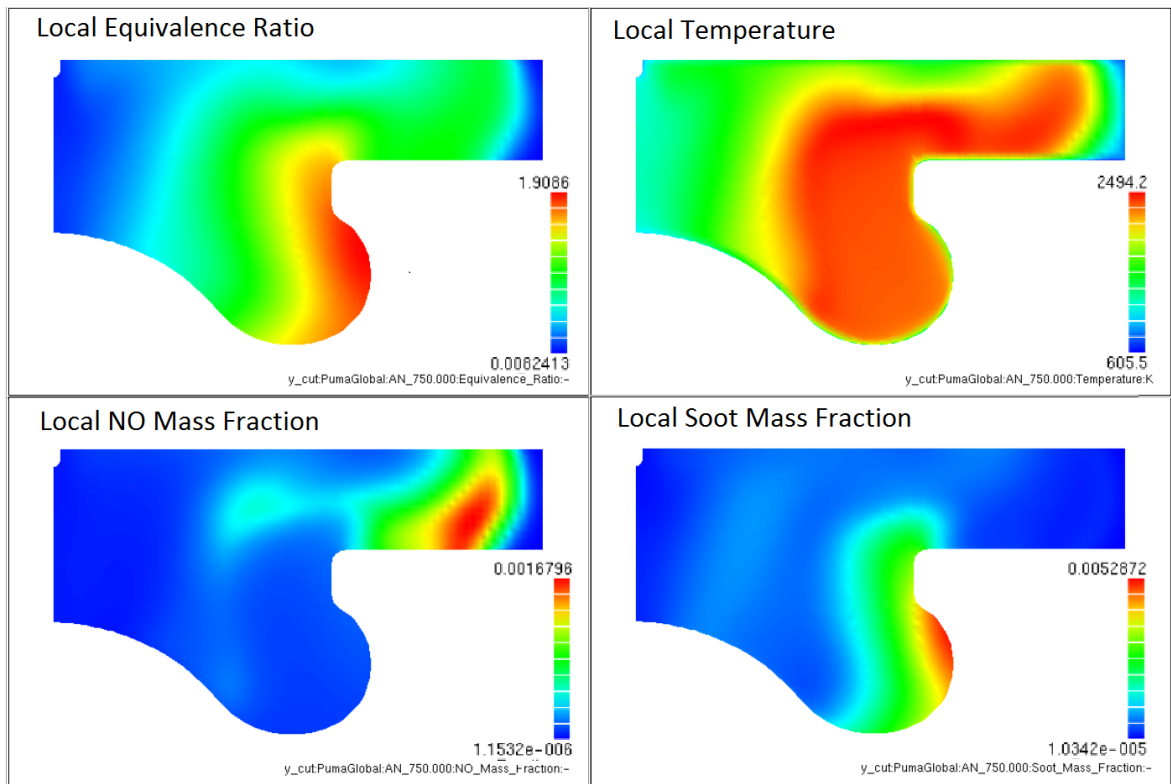


Figure 5.16. Quantity contours at 750 CA.

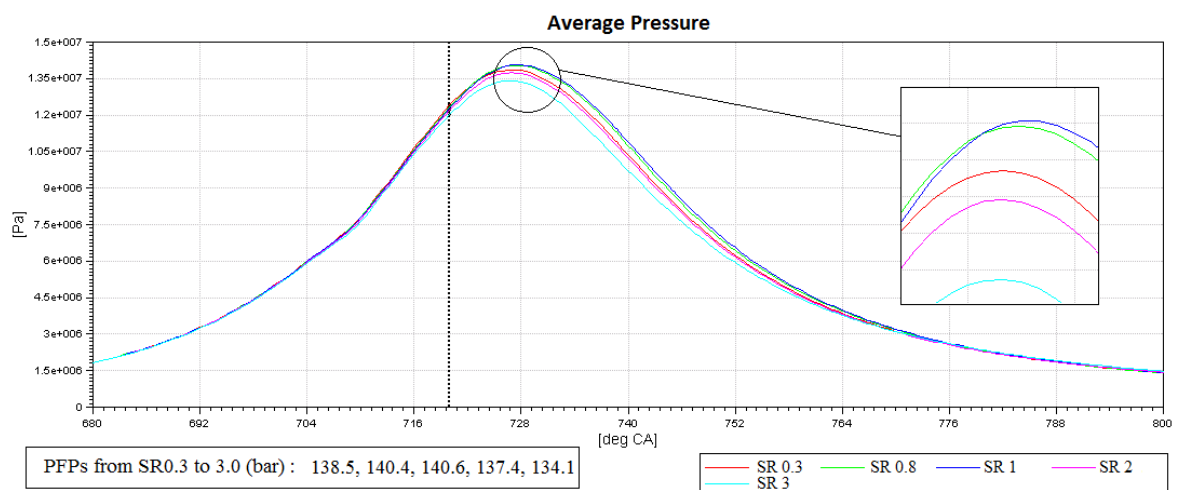


Figure 5.17. Pressure curves for various swirl ratios.

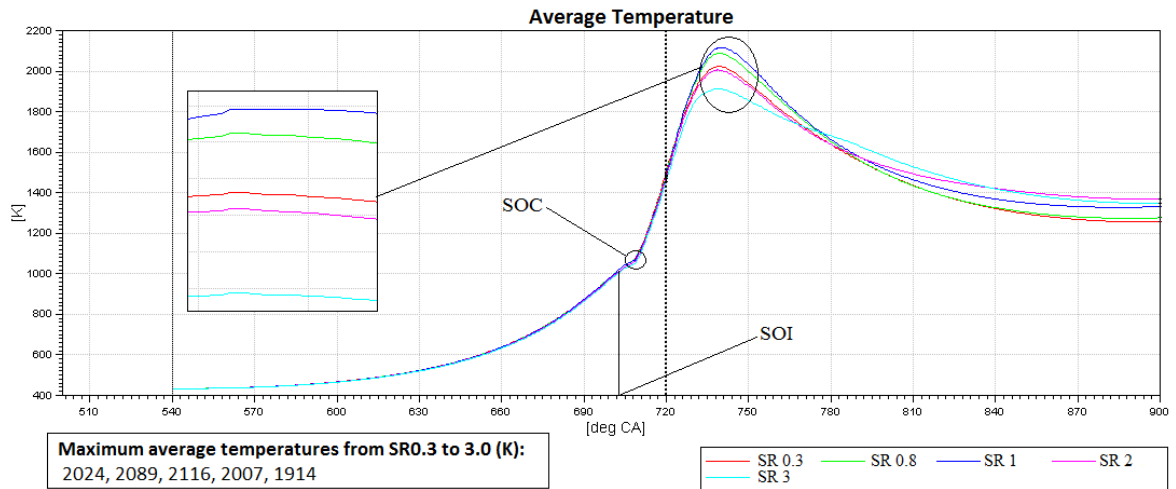


Figure 5.18. Temperature curves for various swirl ratios.

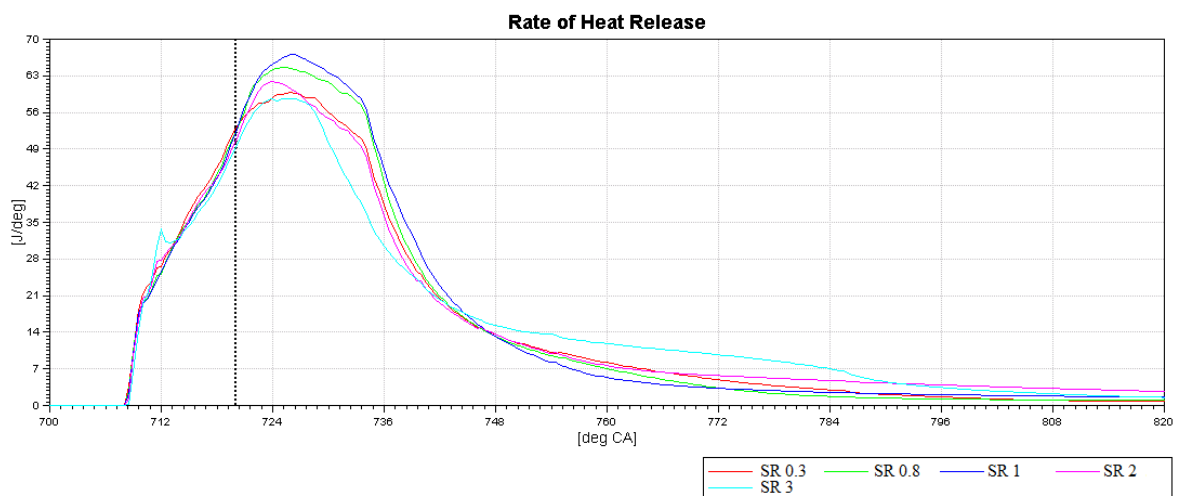


Figure 5.19. Rate of heat release curves for various swirl Ratios.

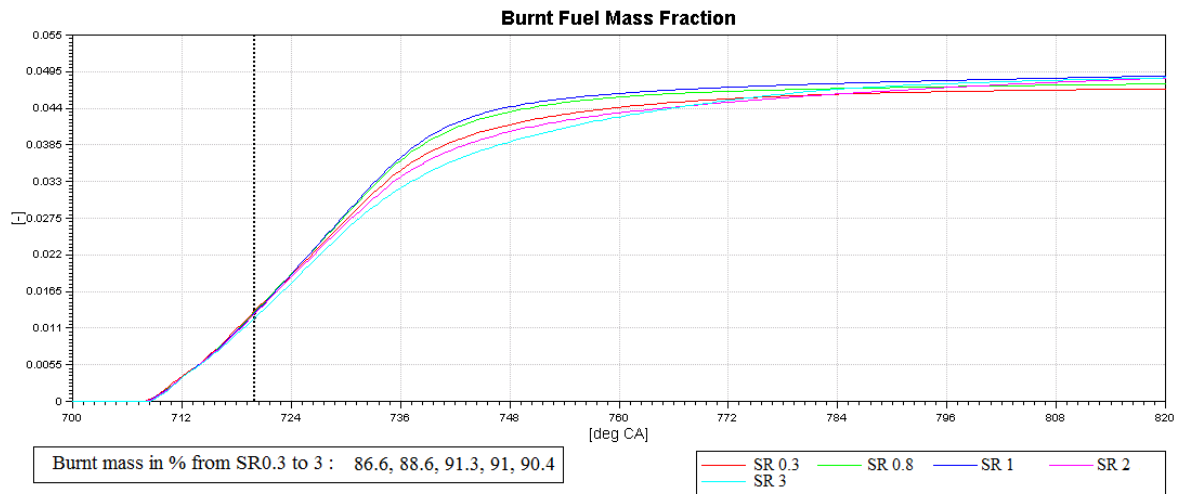


Figure 5.20. Burnt fuel mass fraction curves for various swirl ratios.

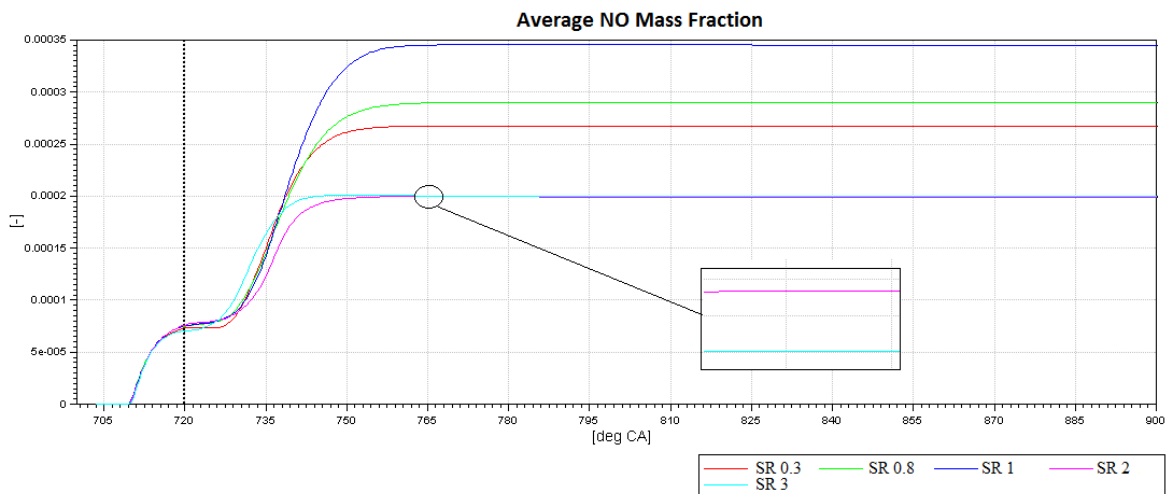


Figure 5.21. NO mass fraction curves for various swirl ratios.

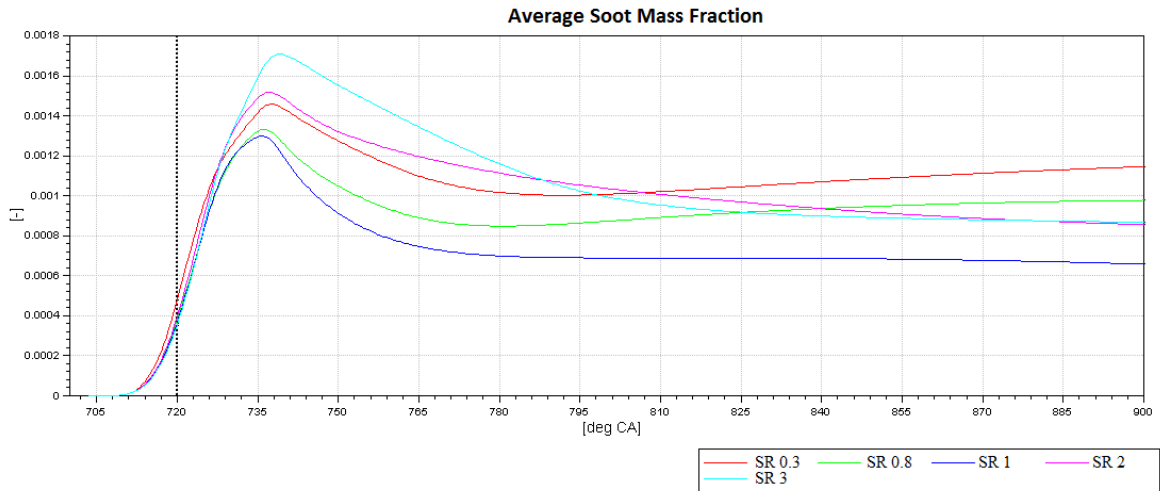


Figure 5.22. Soot mass fraction curves for various swirl ratios.

increasing swirl ratios from SR 0.3 to SR 3.0. The expectation was that the in-cylinder pressure, temperature, heat release and NO mass fraction would show an increasing trend from SR 0.3 to SR 3.0 since it was considered that the increasing swirl motion would provide more homogeneous air-fuel mixture in the cylinder. However, simulation results show a different trend. Increasing swirl ratio contributes the air-fuel mixture till a certain threshold. When the swirl ratio is further increased, then it deteriorates the air-fuel mixing since at excessive swirl ratios, fuel droplets come together and form bigger droplets which adversely affects the in-cylinder charge homogeneity.

Figure 5.17 shows the average pressure values for each swirl ratio. It can be seen that from SR 0.3 to SR 1.0 the PFP values increase and then it shows a decreasing trend from SR 1.0 to SR 3.0. The highest peak firing pressure, 140.6 bars, is achieved at SR 1.0 case. The same trend is observed for average temperature curves in Figure 5.18. Maximum in-cylinder average temperature values rises till SR 1.0 then it, similarly, decreases as the swirl ratio increases. It is read as 2116K for SR 1.0 case, it is 1914 K for SR 3.0 case.

Figure 5.19 shows the rate of heat release for each case. The highest rate of heat release is achieved for SR 1.0 case. There is a similar trend in the rate of heat release curves as for temperature and pressure curves. Burnt mass fraction curves in Figure 5.20 shows that case SR 1.0 has greater efficiency in terms of burnt fuel fraction(91.3%).

It is prevalent that the NO emissions are highly temperature-dependent. As it can be predicted from the average temperature curves in Figure 5.18, the NO formation trends resemble with the temperature change trends. In that sense, within the region from SR 0.3 to SR 1.0 where average temperatures shows an increasing manner, NO formation is expected to rise and similarly with decreasing average temperatures from SR 1.0 to SR 3.0, NO formation is expected to decrease. The prediction done above has been proved by the simulation result. Fig 5.21 indicates the NO mass fractions for each case. It can be understood from Figure 5.22 that increasing swirl ratio degrades the air-fuel mixing when it exceeds SR 1.0 which, in turn, leads to higher soot emissions.

From the all above, considering that the highest temperatures and heat releases and lowest soot emissions are achieved for SR 1.0, it could be said that SR 1.0 provides best fuel-air mixing conditions among the others for the engine that is modeled. Note that optimum swirl ratio depends on engine geometry and operating conditions. Thus, SR 1.0 has been proved to provide better mixing condition for this particular engine and operating conditions.

5.4.2. Simulation Results for Injection Timing

The simulation has been performed to study the influence of fuel injection timing on combustion and emission characteristics. The start of injection (SOI) 21 CA, 17 CA and 13 CA bTDC have been set for the investigation. Note that start of injection at 17 CA bTDC is the base model. Thus, the SOI 21CA and 13 CA bTDC are called advanced and retarded injection, respectively.

The advanced injection timing shows higher PFP and higher maximum in-cylinder average temperature and retarded injection shows lower PFP and lower maximum in-cylinder average temperature with respect to the reference case. As the injection time is advanced, in-cylinder pressure and temperature is not sufficient to ignite the fuel. Thus, a large amount of evaporated fuel is accumulated during the ignition delay period, which leads the first stage of diesel combustion, premixed phase where maximum increase in pressure, temperature and heat release are observed, to become more effective. In retarded injection, the ignition delay period is narrower with reference to the advanced injection and as a result relatively small amount of evaporated fuel is gathered inside the cylinder. It can be seen in Figure 5.23 and Figure 5.24 that as the injection timing is advanced, the PFP and maximum in-cylinder average temperature values increase. Ignition delay times for advanced, reference and retarded injection are, in order, 0.28ms, 0.23ms and 0.18ms.

Rate of heat release curves have been shown in Figure 5.25. In this case, considering the part of the cycle around TDC where maximum temperatures and pressures are observed, although maximum heat release rate diminishes as the injection is advanced, the area under the each curves, which means the accumulated heat release, shows an increasing manner. Figure 5.26 shows the accumulated heat release for each injection timing case. As a result of this, higher temperatures and pressures are observed in advanced injection with respect to the others. Figure 5.27 and 5.28 shows NO and soot mass fraction with respect to crank-angle. Parallel to the temperature trends, NO mass fraction increases as the injection timing is advanced. Contrary to the NO trends, soot mass fraction shows an increasing trend as the injection timing is retarded. Table 5.9 summarizes the general engine outputs for each injection timing.

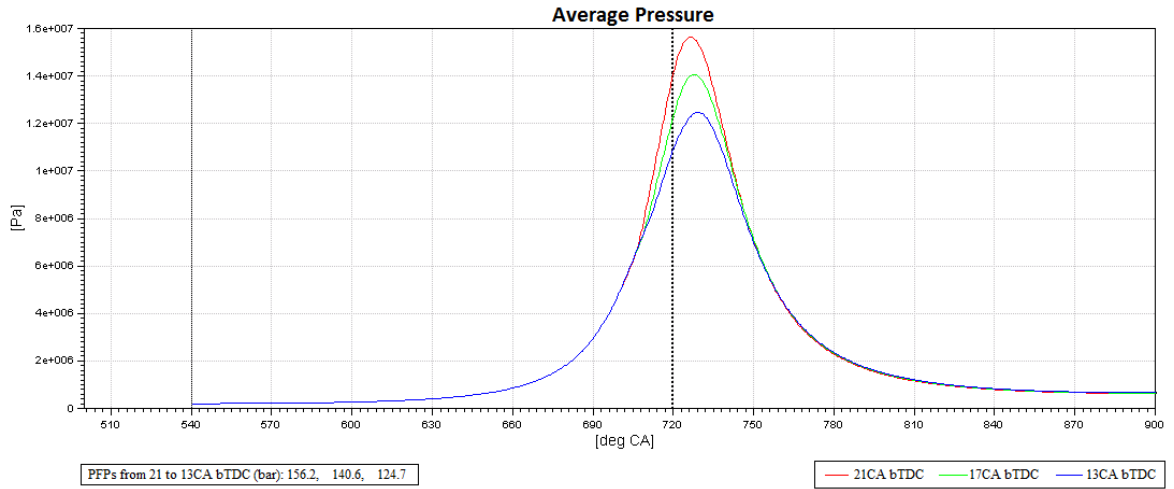


Figure 5.23. Pressure curves for various injection timings.

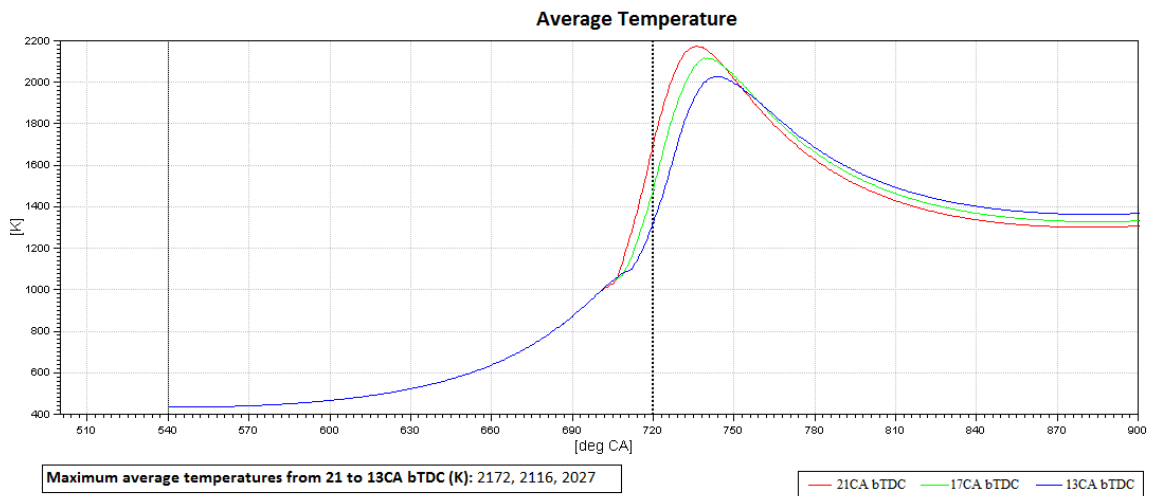


Figure 5.24. Temperature curves for various injection timings.

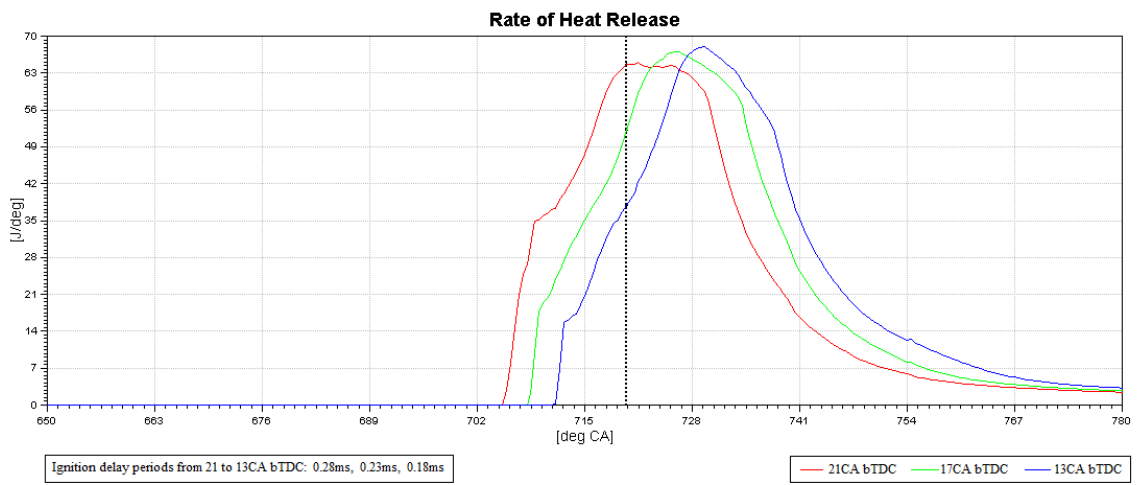


Figure 5.25. Rate of heat release curves for various injection timing.

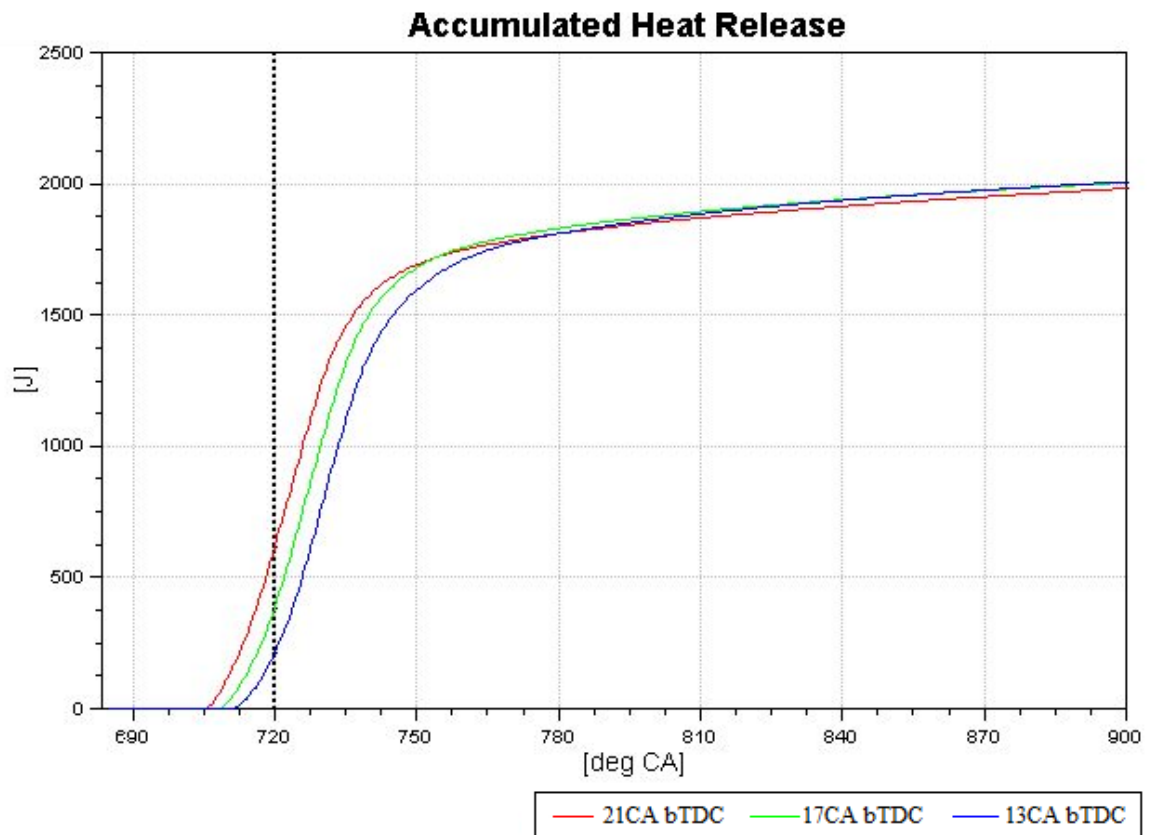


Figure 5.26. Accumulated heat release for various injection timing.

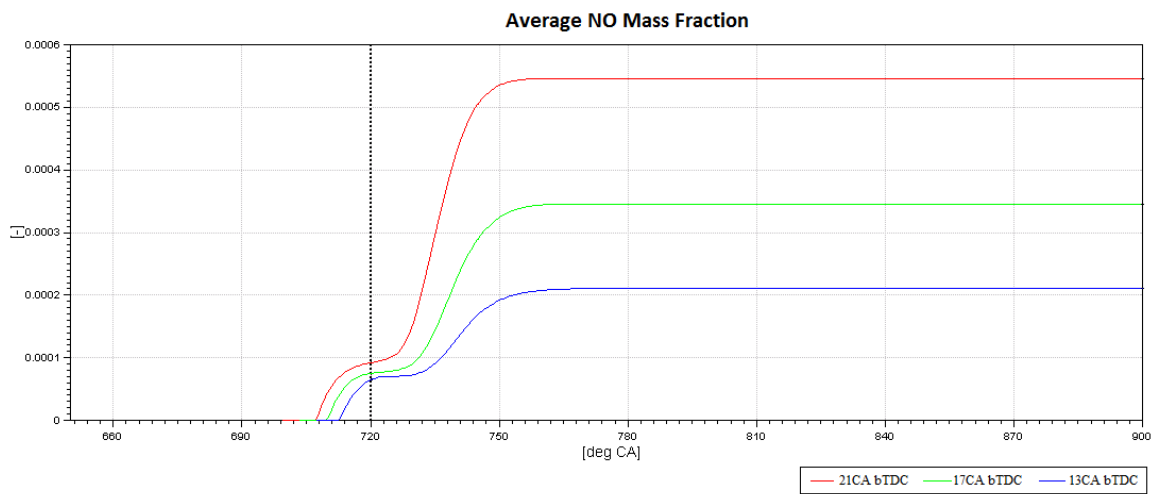


Figure 5.27. NO mass fraction curves for various injection timing.

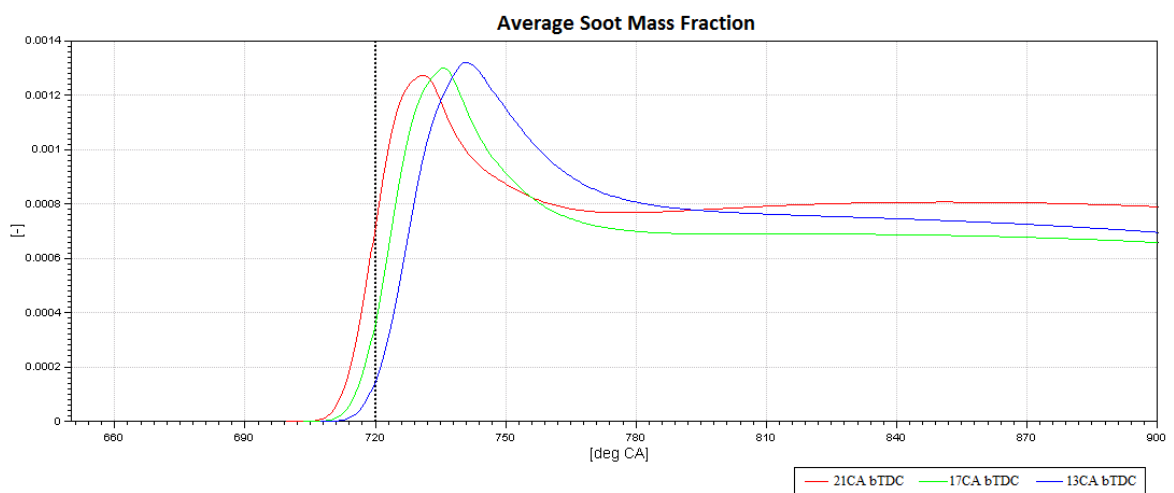


Figure 5.28. Soot mass fraction curves for various injection timing.

Table 5.9. General engine output comparison for injection timing.

Injection timing [CA bTDC]	21	17	13
A/F Ratio [-]	18.32	18.32	18.32
Injected Fuel Mass [mg]	51.5	51.5	51.5
BMEP [bar]	14.71	14.76	14.35
Bsfc [kg/kW h]	229.4	228.6	235.2
Indicated Efficiency [%]	39	39	38
Indicated Power [kW]	25.25	25.34	24.65
NO mass fraction [$\times 10^{-4}$]	5.44	3.45	2.16
Soot mass fraction [$\times 10^{-3}$]	0.79	0.66	0.7

6. CONCLUSION AND FUTURE WORK

In this study, multidimensional CFD approach has been used to simulate a 2.2 liter CI diesel engine in order to investigate the influence of varying swirl ratio and injection timing. The combustion process in diesel engines is highly controlled by the injection and swirl motion in the cylinder since fuel-air mixing quality is mainly dependent on those parameters. Varying swirl ratios from 0.3 to 3.0 have been set for simulation. The expectation was that the increasing swirl, the rotational motion of the in-cylinder charge about the cylinder axis, would improve the air-fuel mixing process and it would, in turn, lead to more efficient combustion and higher BMEP. However, it has been found that after a certain point, increasing swirl ratio shows negative effect on combustion. For this particular engine, it has been observed that the optimum swirl ratio is 1.0 among the others. As the swirl ratio gets increased over its optimum range, it worsens the combustion which is possibly caused by the faster in-cylinder flow motion which leads to higher convective heat transfer through the cylinder walls. In the study of Manimaran et al. [8] it has been found that excessive swirl ratios result in higher spray Sauter mean diameter(SMD). It has been claimed that SMD increases for swirl ratios of 3.2 and 4.1 twice in proportion to swirl ratios of 1.4 and 2.3 as it is shown in Figure 6.1. Thus, another reason might be that the excessive swirl motion leads liquid fuel droplets to combine and form larger fuel droplets which adversely affect the air-fuel mixing and the combustion. Table 6.1 shows that average convection heat flux through cylinder wall gets higher as swirl ratio values increase. As for the injection timing, it was predicted that the advanced injection timing would elevate the in-cylinder temperature and pressure which result in higher work output since it provided longer ignition delay period for air-fuel mixing. However, the simulation results show that it has an optimum. Baseline injection timing provides the best indicated power output as retarded injection gives the lowest soot emissions. It has also been found that the NO emission formation and in-cylinder average temperature level are directly proportional. It has been also observed that there is an inverse proportion between NO and soot emission (formed in premixed combustion) level. In short, the higher in-cylinder temperature gets, the higher NO emissions and the lower soot emissions become.

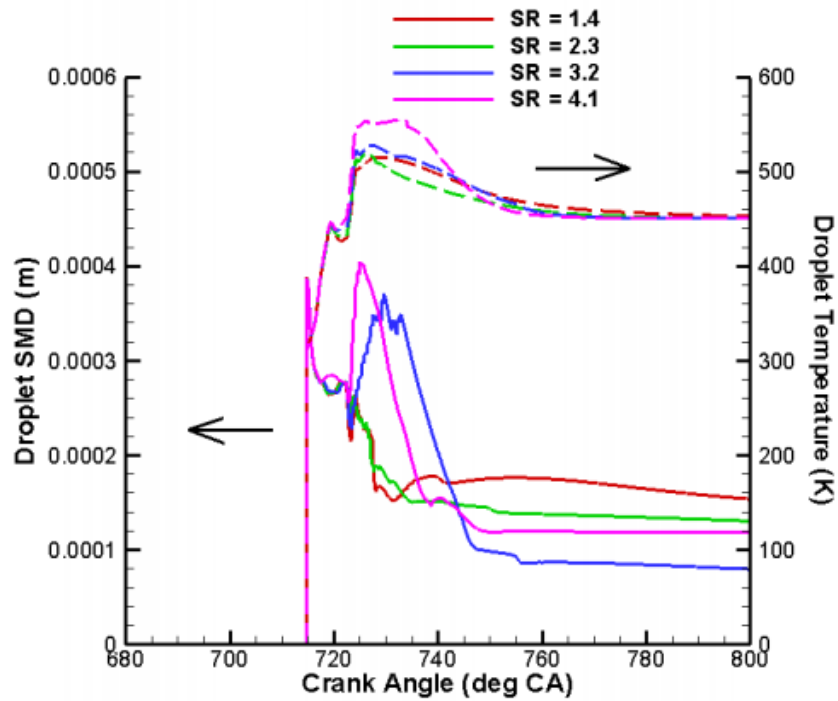


Figure 6.1. SMD for various swirl ratios [8].

Table 6.1. Average convective wall heat flux for SR cases.

Case Name	Average Convective Wall Heat Flux [W/CA]
SR 0.3	-18317.24
SR 0.8	-18554.78
SR 1.0	-18825.72
SR 2.0	-18929.68
SR 3.0	-21213.83

The present study focuses only on some portion of the entire four cycle, which covers only the compression and the expansion strokes. Thus, it could be further extended to gain deeper insights for diesel combustion by including the intake and exhaust strokes to investigate the effect of those cycles on in-cylinder conditions. Furthermore, other critical components for diesel engine such as EGR, SCR and DPF could be taken into account since they play a key role on the final NO and soot emissions from the engine. Split injection could also be studied to simulate the effect of pre-injection and post-injection on engine performance and emissions. Radiation heat transfer has been excluded from this study since it is too complex and it requires more advanced computational power. With the advent of powerful computer technology, the radiation heat transfer models could be integrated into the combustion simulations.

REFERENCES

1. “EAMA World Motor Vehicle Production”, 2014, <http://www.acea.be/statistics>, accessed at June 2015.
2. “EPA Where the Energy Goes: Gasoline Vehicles”, 2014, <https://www.fueleconomy.gov>, accessed at August 2015.
3. Heywood, J. B., *Internal combustion engine fundamentals*, Vol. 930, McGraw-hill New York, 1988.
4. Kolmanovsky, I., P. Morall, M. Van Nieuwstadt and A. Stefanopoulou, “Issues in modelling and control of intake flow in variable geometry turbocharged engines”, *Chapman and Hall CRC research notes in mathematics*, pp. 436–445, 1999.
5. Luckhchoura, V., *Modeling of injection-rate shaping in diesel engine combustion*, Ph.D. Thesis, Aachen, Techn. Hochsch., Diss., 2010, 2010.
6. AVL LIST GmbH, *AVL FIRE Combustion Module, User Manual*, 2013.
7. Bravo, L. and C.-B. Kweon, *A Review on Liquid Spray Models for Diesel Engine Computational Analysis*, Tech. rep., DTIC Document, 2014.
8. Manimaran, R. and R. Thundil Karuppa Raj, “Computational studies of swirl ratio and injection timing on atomization in a direct injection diesel engine”, *Frontiers in Heat and Mass Transfer (FHMT)*, Vol. 5, No. 1, 2014.
9. Ho, R., M. Yusoff and K. Palanisamy, “Trend and future of diesel engine: Development of high efficiency and low emission low temperature combustion diesel engine”, *IOP Conference Series: Earth and Environmental Science*, Vol. 16, p. 012112, IOP Publishing, 2013.

10. Reitz, R. D., “Directions in internal combustion engine research”, *Combustion and Flame*, Vol. 160, No. 1, pp. 1–8, 2013.
11. Hountalas, D. T., T. Zannis and G. Mavropoulos, *Potential benefits in heavy duty diesel engine performance and emissions from the use of variable compression ratio*, Tech. rep., SAE Technical Paper, 2006.
12. Wang, D. and C. Zhang, “Development of a Real-Time NO_x Prediction Model Based on Heat Release Analysis in a Direct-Injection Diesel Engine”, *Journal of Engineering for Gas Turbines and Power*, Vol. 136, No. 3, p. 034501, 2014.
13. Wei, S., F. Wang, X. Leng, X. Liu and K. Ji, “Numerical analysis on the effect of swirl ratios on swirl chamber combustion system of DI diesel engines”, *Energy Conversion and Management*, Vol. 75, pp. 184–190, 2013.
14. Tatschl, R. and P. Priesching, “3D-CFD Simulation of DI-Diesel engine combustion and pollutant formation”, *University of Pitesti Scientific Bulletin Faculty of Mechanics and Technology Automotive series, year XVI*, , No. 20, 2009.
15. Rao, V. and D. Honnery, “A comparison of two NO_x prediction schemes for use in diesel engine thermodynamic modelling”, *Fuel*, Vol. 107, pp. 662–670, 2013.
16. Mellor, A. M., J. Mello, K. P. Duffy, W. Easley and J. Faulkner, *Skeletal mechanism for NO_x chemistry in diesel engines*, Tech. rep., SAE Technical Paper, 1998.
17. Rakopoulos, C., G. Kosmadakis and E. Parriotis, “Investigation of piston bowl geometry and speed effects in a motored HSDI diesel engine using a CFD against a quasi-dimensional model”, *Energy conversion and management*, Vol. 51, No. 3, pp. 470–484, 2010.
18. Magnussen, B. F. and B. H. Hjertager, “On mathematical modeling of turbulent combustion with special emphasis on soot formation and combustion”, *Symposium (International) on Combustion*, Vol. 16, pp. 719–729, Elsevier, 1977.

19. Patterson, M., S.-C. Kong, G. Hampson and R. D. Reitz, *Modeling the effects of fuel injection characteristics on diesel engine soot and NO_x emissions*, Tech. rep., SAE Technical Paper, 1994.
20. Metghalchi, M. and J. C. Keck, “Burning velocities of mixtures of air with methanol, isooctane, and indolene at high pressure and temperature”, *Combustion and flame*, Vol. 48, pp. 191–210, 1982.
21. Meneveau, C. and T. Poinso, “Stretching and quenching of flamelets in premixed turbulent combustion”, *Combustion and Flame*, Vol. 86, No. 4, pp. 311–332, 1991.
22. Showry, K. B., A. Raju and P. R. Reddy, “Multi-Dimensional Modeling of Direct Injection Diesel Engine and Effects of Split Injection”, *International Journal of Scientific and Research Publications*, Vol. 2, p. 74, 2012.
23. Hiroyasu, H., T. Kadota and M. Arai, “Development and use of a spray combustion modeling to predict diesel engine efficiency and pollutant emissions: Part 1 combustion modeling”, *Bulletin of JSME*, Vol. 26, No. 214, pp. 569–575, 1983.
24. Dukowicz, J. K., “A particle-fluid numerical model for liquid sprays”, *Journal of Computational Physics*, Vol. 35, No. 2, pp. 229–253, 1980.
25. Dukowicz, J., *Quasi-steady droplet change in the presence of convection*, LA7997-MS, Tech. rep., Los Alamos, USA: Scientific Laboratory of California, 1979.
26. Liu, A. B., D. Mather and R. D. Reitz, *Modeling the effects of drop drag and breakup on fuel sprays*, Tech. rep., DTIC Document, 1993.
27. Asma, A., *1-D compression ignition engine simulation and comparison of soot emission models*, Master’s Thesis, Bogazici University, Turkey, 2015.